

# Spatially resolved gas-phase metallicity in FIRE-2 dwarfs: late-time evolution of metallicity relations in simulations with feedback and mergers

Lori E. Porter <sup>1</sup>★, Matthew E. Orr <sup>2,3</sup>, Blakesley Burkhardt <sup>2,3</sup>, Andrew Wetzel <sup>4</sup>, Xiangcheng Ma <sup>5</sup>, Philip F. Hopkins <sup>6</sup> and Andrew Emerick <sup>6,7</sup>

<sup>1</sup>Department of Physics and Astronomy, University of Louisville, 102 Natural Sciences Building, Louisville, KY 40292, USA

<sup>2</sup>Department of Physics and Astronomy, Rutgers, The State University of New Jersey, 136 Frelinghuysen Rd, Piscataway, NJ 08854, USA

<sup>3</sup>Center for Computational Astrophysics, Flatiron Institute, 162 Fifth Avenue, New York, NY 10010, USA

<sup>4</sup>Department of Physics and Astronomy, University of California, Davis, CA 95616, USA

<sup>5</sup>Department of Astronomy and Theoretical Astrophysics Center, University of California Berkeley, Berkeley, CA 94720, USA

<sup>6</sup>TAPIR, California Institute of Technology, 1200 E. California Blvd, MC 350-17, Pasadena, CA 91125, USA

<sup>7</sup>Carnegie Observatories, 813 Santa Barbara Street, Pasadena, CA 91101, USA

Accepted 2022 July 7. Received 2022 July 6; in original form 2022 April 6

## ABSTRACT

We present an analysis of spatially resolved gas-phase metallicity relations in five dwarf galaxies ( $M_{\text{halo}} \approx 10^{11} M_{\odot}$ ,  $M_{\star} \approx 10^{8.8} - 10^{9.6} M_{\odot}$ ) from the FIRE-2 (Feedback in Realistic Environments) cosmological zoom-in simulation suite, which include an explicit model for sub-grid turbulent mixing of metals in gas, near  $z \approx 0$ , over a period of 1.4 Gyr, and compare our findings with observations. While these dwarf galaxies represent a diverse sample, we find that all simulated galaxies match the observed mass–metallicity (MZR) and mass–metallicity gradient (MZGR) relations. We note that in all five galaxies, the metallicities are effectively identical between phases of the interstellar medium (ISM), with 95 per cent of the gas being within  $\pm 0.1$  dex between the cold and dense gas ( $T < 500$  K and  $n_{\text{H}} > 1 \text{ cm}^{-3}$ ), ionized gas (near the  $\text{H}\alpha T \approx 10^4$  K ridge-line), and nebular regions (ionized gas where the 10 Myr-averaged star formation rate is non-zero). We find that most of the scatter in relative metallicity between cold dense gas and ionized gas/nebular regions can be attributed to either local starburst events or metal-poor inflows. We also note the presence of a major merger in one of our galaxies, **m11e**, with a substantial impact on the metallicity distribution in the spatially resolved map, showing two strong metallicity peaks and triggering a starburst in the main galaxy.

**Key words:** ISM: abundances – ISM: kinematics and dynamics – galaxies: dwarf – galaxies: evolution – galaxies: ISM.

## 1 INTRODUCTION

Dwarf galaxies are one of the most important components of galactic evolution. They are the lowest mass galaxies, but are the most abundant type, and form the bottom of the hierarchy of galactic evolution. At low masses, the effects of individual starburst events are particularly pronounced since they can perturb the entire existing gas reservoir in the galaxy. As a result, dwarf galaxies are ideal testbeds for analysing various forms of enrichment and implementations of feedback (Tolstoy, Hill & Tosi 2009; Simon 2019).

Gas-phase metallicity enrichment is essential to our understanding of galactic formation and evolution. The metal enrichment that follows supernovae (SNe) surrenders information about the star formation history (Tolstoy et al. 2009; Sacchi et al. 2016) and the assembly history of galaxies (Sawala et al. 2010; Pawlik, Milosavljević & Bromm 2013; Hirschmann, De Lucia & Fontanot 2016). When metals are distributed throughout the interstellar medium (ISM) by SNe, these metals constrain recent and integrated star formation and trace feedback from massive stars. These stellar byproducts also influence galactic evolution. In particular, the gas-

phase oxygen abundance in ionized gas is significant, as oxygen is the most abundant metal element, and a primary coolant of the ISM (Draine 2011). It produces strong optical emission lines when ionized and is used as a tracer of metallicity in the ISM (e.g. Sánchez et al. 2019).

One of the most well-known relationships for galaxy evolution and oxygen abundance is the mass–metallicity relation (MZR). This relation is the strong correlation between stellar mass and both the gas-phase metallicity and stellar metallicity (Gallazzi et al. 2005; Kewley & Ellison 2008; Lee, Bell & Somerville 2008; Kirby et al. 2013; Jimmy et al. 2015; Ma et al. 2016; Hidalgo 2017; Maiolino & Mannucci 2019); more massive galaxies tend to have higher metal enrichment than their low-mass counterparts (i.e. dwarf galaxies). Kirby et al. (2013) rationalizes the MZR by arguing that the deeper potential wells of more massive galaxies more easily retain metals, as they produce them through *in situ* star formation. Dwarf galaxies, such as the ones in this study, often have shallower potential wells that make feedback more effective at removing metals from the ISM, allowing for the gas-phase metal reservoirs to be depleted in samples of dwarf galaxies as compared to their more massive counterparts. In addition, lower mass galaxies are typically more gas-rich, resulting in diluted metals in the case that they are retained. However, we note that mechanisms in dwarf galaxies are diverse, as

\* E-mail: leport01@louisville.edu

there are some unusual cases where dwarf galaxies do not produce winds that aid in expelling their metals, detailed by Romano et al. (2019).

Dilution is only one of the possible drivers of the MZR (Maiolino et al. 2008). One potential way to derive the MZR relies on ‘galaxy downsizing’, an argument that more massive systems have shorter gas depletion times, resulting in a metallicity relation with stellar mass at any given redshift (Finlator & Davé 2008; Maiolino et al. 2008; Pérez-González et al. 2008; Calura et al. 2009; Maier et al. 2015; Maiolino & Mannucci 2019; Spitoni et al. 2020). Hirschmann et al. (2016) also propose a connection between the MZR and differential outflows, caused by bursty star formation at high redshifts when star formation is at its peak. In addition, similar to the process caused by galactic outflows, Dalcanton (2007) suggests a similar relationship with galactic inflows that cause a differential dilution. It is also possible that the MZR can be affected by a variable integrated stellar initial mass function (IMF) as depicted by Köppen, Weidner & Kroupa (2007), although they utilize a closed-box model.

Similarly, star formation efficiency also has a role to play in the MZR, as galaxies that have increased star formation rates (SFRs) will reach a higher stellar mass and metallicity enrichment. The stellar mass–halo mass relation presented in Behroozi, Wechsler & Conroy (2013) and Moster, Naab & White (2013) suggests that lower SFR efficiency in dwarf galaxies results in less metal enrichment. Hopkins et al. (2013) also find that the presence of mergers can lower star formation after producing starbursts. For the masses relevant to this study ( $M_* \approx 10^{8.75} - 10^{9.75} M_\odot$ ; see Fig. 1), the MZR can typically be characterized by a power law. Lee et al. (2006) support this, confirming that a tight correlation exists among local galaxies with stellar masses from  $10^6$  to  $10^{11} M_\odot$ .

In addition to the MZR, gas-phase metallicity gradients in dwarf galaxies can contribute insight into galaxy assemblies and provide information as to how ordered the systems are. This is because metals are not uniformly distributed throughout a galaxy (Shaver et al. 1983). Instead, feedback has a predominant role to play in the distribution of metals throughout a galaxy (Pilkington et al. 2012; Hemler et al. 2021). For example, Gibson et al. (2013) use cosmological hydrodynamical simulations to investigate how feedback affects the distribution of metals in disc galaxies, finding that flat and negative gradients are common in galaxies with strong feedback redistributing metals. In contrast, simulations with weaker feedback tend to produce steeper gradients. Hemler et al. (2021) also find that many TNG50 galaxies ( $10^{10} M_\odot \leq M_* \leq 10^{10.5} M_\odot$ ) also exhibit negative gradients around  $z \approx 0$ , although they note that TNG50 gradients tend to be steeper at higher redshifts than similar galaxies in the FIRE (Feedback In Realistic Environments) simulations.

Sharda et al. (2021) found the metallicity gradient measured in dex per kpc has either one of two properties at stellar mass of  $M_* \sim 10^{10-10.5} M_\odot$ : it will be independent of stellar mass up to this point, then flatten towards zero at higher stellar masses, exactly the opposite as found in FIRE-2 (Mercado et al. 2021), or it will have a mild curvature with flat gradients on either side (e.g. Belfiore et al. 2017). Further investigation into the physical cause of the difference in gradients, similar to the MZR, can provide clues as to how feedback and turbulence can affect the population of galaxies at a lower mass, and how dwarf galaxies lose their metals (Dekel & Silk 1986; Dalcanton 2007; Burkhardt et al. 2010; Ma et al. 2016). In addition, the expectation that MW-mass disc galaxies exhibit negative radial metallicity gradients provides evidence of inside-out galaxy formation (Mo, Mao & White 1998; Pilkington et al.

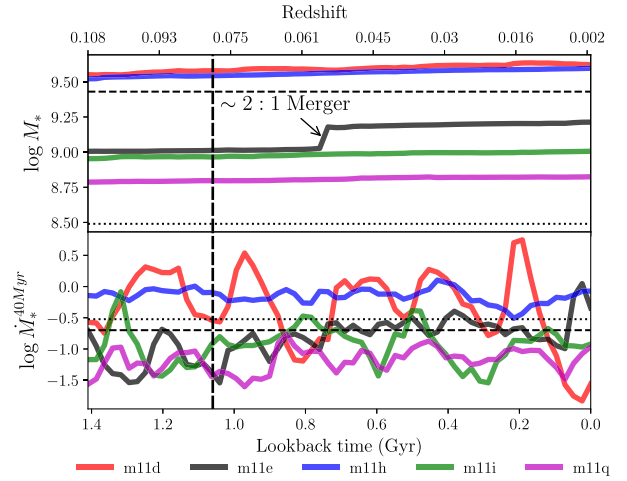


**Figure 1.** *Top panel:* Stellar masses in each snapshot, over the entire analysis period ( $t_{\text{lookback}} = 1.4$  Gyr to  $t_{\text{lookback}} = 0$  Gyr), for all five FIRE-2 dwarf galaxies. Stellar masses exhibit a slight steady growth over time. **m11e** (black) is an exception, with disturbances due to a merger. SMC/LMC masses from Bekki & Stanimirović (2009) and van der Marel et al. (2002) for reference are denoted by the horizontal dotted and dashed black lines, respectively. *Bottom panel:* Star formation rates averaged over the last 40 Myr for each snapshot. **m11d** is clearly bursty with variations over 2 dex. **m11e** has a merger-triggered starburst around  $t_{\text{lookback}} = 0$  Gyr. **m11i** is somewhat bursty with variations over 0.5 dex. **m11h** and **m11q** are fairly smooth with recent star formation history. Thickly dashed vertical line denotes  $t_{\text{lookback}} = 0.36$  Gyr, which corresponds to the particular snapshot shown in Figs 2 and 3. The recent averaged SMC star formation rate from observations (primarily in the UV) is denoted by the black dotted line (Rezaei Kh. et al. 2014; Rubele et al. 2015; Hagen et al. 2017). A similar recent averaged SFR for the LMC is represented by the black dashed line (Harris & Zaritsky 2009; Rezaei Kh. et al. 2014). All five simulations appear to be in good agreement with observations.

2012; Sharda et al. 2021). This is found in Magrini et al. (2016)’s observations and Bellardini et al. (2021)’s azimuthal analysis in the FIRE-2 MW and M31-mass galaxies. However, as found in Mercado et al. (2021), dwarf galaxies behave differently due to their usually well-mixed ISM. Dwarf galaxies have the tendency to exhibit no radial gradients, but this varies across galaxies of similar masses (Belfiore et al. 2017; Ma et al. 2017; Escala et al. 2018; Mercado et al. 2021).

Cosmological zoom-in simulations are an excellent choice to study the metallicity distributions in dwarf galaxies. Several studies in this field have used one-zone models (Lanfranchi & Matteucci 2003, 2007, 2010; Yin, Matteucci & Vladilo 2011), but rely on simplistic models of feedback. While these models can be effective, they lack the cosmological context surrounding specific galaxies (e.g. the highly variable rates of mergers or inflows) and the non-linear interactions between stellar feedback within galaxies and their surroundings (Ma et al. 2016; Escala et al. 2018). This makes predicting metallicity gradients difficult in such models (they are necessarily ‘sub-grid’ with a single zone), and they fail to address temporal scatter in the MZR and gradients. Semi-analytical galaxy formation models (SAMs) are also used to study chemical evolution in cosmological contexts, as demonstrated with local dwarfs in Calura & Menci (2009) and Yates et al. (2013). These models allow for the implementation of a realistic background for star formation histories and mass assembly. However, as noted by Romano & Starkenburg (2013), they often lack diverse forms of feedback that affect the evolution of certain metals. The increased dynamic range found in cosmological zoom-in simulations is required to reproduce

**Table 1.** Summary of  $z \approx 0$  properties of the FIRE-2 dwarf galaxies used in this work.

Name	$\log(\frac{M_\star}{M_\odot})$	$\log(\frac{M_{\text{gas}}}{M_\odot})$	$\frac{R_{\star,1/2}}{\text{kpc}}$	$\frac{R_{\text{gas},1/2}}{\text{kpc}}$	$\frac{v_c}{\text{km s}^{-1}}$ <sup>a</sup>
m11d <sup>b</sup>	9.6	9.5	7.0	11.4	85.6
m11e	9.2	9.3	3.9	6.6	82.7
m11h	9.6	9.6	4.1	6.3	97.7
m11i	9.0	9.2	3.8	3.4	53.1
m11q	8.8	9.2	2.6	4.2	68.8

Notes. all quantities measured within a 30 kpc cubic aperture.

<sup>a</sup>Circular velocities evaluated at  $R_{\text{gas},1/2}$ .

<sup>b</sup>**m11d** is significantly disrupted at  $z \approx 0$  from a recent starburst (see e.g. Fig. 2), as such its radius (and  $v_c$  at that radius) is poorly defined.

All galaxies here are introduced by El-Badry et al. (2018), with the exception of **m11q**, which is introduced by Hopkins et al. (2018).

observed stellar masses, SFRs, and metallicities in dwarf galaxies (Romano & Starkenburg 2013; Ma et al. 2016; Hemler et al. 2021).

This paper combines the powerful attributes of dwarf galaxies, the FIRE-2 simulations, and metal enrichment to form an analysis of gas-phase metallicity relations in this galaxy mass range. By combining all of these tools, we are effectively able to resolve the internal structures of galaxies while maintaining realistic cosmological context, using FIRE’s ability to resolve a multiphase ISM, and include detailed star formation, stellar feedback, and other forms of physics that result in successfully reproducing observations. In this paper, we analyse five dwarf galaxies from the FIRE-2 simulations near  $z \approx 0$ , allowing for a specific focus on the MZR in the local Universe, a redshift range with ample comparable observations.

This paper is organized as follows. First, in Section 2, we review and introduce our analysis methods of the FIRE-2 simulations. In Section 3, we discuss our results, including finds related to the MZR, metallicity profiles, and galaxy mergers. This paper is then concluded by a discussion of our findings compared to existing literature and observations in Section 4, and summarizing our results in Section 5.

## 2 SIMULATIONS AND METHODS

In our analysis, we make use of five dwarf galaxies from the FIRE-2 cosmological zoom-in simulation suite (Hopkins et al. 2018). As described in Hopkins et al. (2018), FIRE-2 utilizes a standard, flat  $\Lambda$  cosmological model where  $h \sim 0.70$ ,  $\Omega_M = 1 - \Omega_\Lambda \sim 0.27$ , and  $\Omega_b = 0.045$ . These galaxies have halo masses  $\sim 10^{11} M_\odot$ , and stellar masses spanning from  $\sim 2 \times$  the SMC mass ( $10^{8.5} M_\star$ ; Bekki & Stanimirović 2009) to slightly more massive than the LMC ( $10^{9.4} M_\star$ ; van der Marel et al. 2002; see Table 1 for a summary of the  $z \approx 0$  galaxy masses, sizes, and rotational velocities). We use approximately 60 snapshots from each simulation, spaced  $\sim 25$  Myrs in time (for a roughly 1.4 Gyr total period analysed) near  $z \approx 0$  (specifically,  $0 < z < 0.11$ ). This redshift range correlates with the local Universe, providing an opportunity to compare with observations on similar Local Group dwarf galaxies, such as those found in Tremonti et al. (2004), Belfiore et al. (2017), and Sánchez et al. (2019), which use redshifts of  $z \sim 0.1$ ,  $0.01 < z < 0.15$ , and  $0.005 < z < 0.1$ , respectively. For a more complete formation history of these five dwarf galaxies, we direct the reader to El-Badry et al. (2018) and Hopkins et al. (2018).

We generate mock observational maps from these snapshots with the same method as Orr et al. (2020): we project the dwarf galaxies face-on using the net angular momentum vector of the star particles within a 3D stellar half-mass radius, and binning star particles and gas elements into square pixels with side-lengths (i.e. ‘pixel sizes’)

250 pc, a size which accurately resolves the internal gas structures of the simulated galaxies (Orr et al. 2020), and corresponds with the angular resolution of a number of observational surveys (Belfiore et al. 2017). The maps are 30 kpc on a side and integrate gas and stars within  $\pm 15$  kpc of the identified galactic mid-plane. This cube includes all of the galaxy body and much of the surrounding warm gas halo for all five of the dwarf galaxies that we map. One simulation however, **m11e**, undergoes a major ( $\sim 2:1 M_\star$ ) merger in the analysis period; to capture the interaction of the two warm gas haloes surrounding the main galaxy and its companion, we expand the size of the mapping cube to 60 kpc on a side (and  $\pm 30$  kpc along the line of sight).

A detailed presentation of the star formation prescription, feedback physics, and enrichment processes used in these simulations can be found in Hopkins et al. (2018); however, we briefly reiterate some of the relevant implementations here. All these runs have minimum baryonic particle/element masses of  $m_{b,\text{min}} = 7100 M_\odot$ , adaptive force softening (with minimum softening lengths  $< 1$  pc), and a 10 K gas temperature floor. As the softening lengths are adaptive, we point out that the median softening length for the gas elements in these dwarf galaxies is  $h \approx 90$  pc for  $n > 1 \text{ cm}^{-3}$  (and  $h \approx 50$  pc for  $n > 10 \text{ cm}^{-3}$ ). The spatially resolved maps that we produce in our analysis have a pixel size of 250 pc, which more than adequately resolves the cold and dense turbulent gas structures (these have softening lengths  $\ll 50$  pc). The warm diffuse ionized gas in the galactic outskirts is marginally resolved at this pixel size, but our analysis focuses primarily on the better (spatially) resolved gas within the primary body of these dwarf galaxies, and this does not qualitatively affect our interpretations of the surrounding warm gas haloes.

In these simulations, star formation proceeds in dense ( $n > 10^3 \text{ cm}^{-3}$ ), molecular (following the scalings of Krumholz & Gnedin 2011), self-gravitating (viral parameter  $\alpha_{\text{vir}} < 1$ ) and Jeans-unstable (below the resolution scale; see section 2.4 of Hopkins et al. 2018) gas, at a rate of  $\dot{\rho}_\star = \rho_{\text{gas}}/t_{\text{ff}}$  (where  $t_{\text{ff}}$  is the free-fall time of the gas element). The resulting star particles are single stellar populations, with a single age, metallicity, and mass. Feedback physics in the forms of supernovae, stellar mass-loss (OB/AGB-star winds), photoionization and photoelectric heating, and radiation pressure are explicitly included. For more details on feedback implementation, see section 2.5 of Hopkins et al. (2018). These simulations do not include black holes (and as such, do not have any AGN feedback).

As we focus heavily on the metal reservoirs of these dwarf galaxies, we summarize here the abundance/enrichment implementation of FIRE-2 (again, see Hopkins et al. 2018 for more detail): nucleosynthetic yields from core-collapse SNe taken from Nomoto et al. (2006), Type-Ia SNe yields from Iwamoto et al. (1999), and stellar wind yields (from O, B, and AGB stars) from Wiersma et al. (2009). These simulations also include a sub-grid metal diffusion model, accounting for turbulent mixing in unresolved eddies (Su et al. 2017; Escala et al. 2018). The diffusion term smooths the abundance distribution following the prescription of Shen, Wadsley & Stinson (2010), resulting in a more realistic distribution of gas phase (and consequently stellar) metallicities (Escala et al. 2018). Escala et al. (2018) further elaborates and concludes that star-forming gas in FIRE-2 dwarf galaxies is typically well-mixed at any fixed time, and the enrichment over time leads to a stellar metallicity distribution that matches observations, which is only achieved when simulations model metal mixing.

We produce proxies for observational metallicity tracers by mapping the ionized gas near the  $\text{H}\alpha T \approx 10^4$  K ridge-line (specifically, we identify this gas in a band of  $|\log T - 4.05| < 1/6$  to reasonably capture the whole  $\text{H}\alpha T \approx 10^4$  K ridge-line), as well as cold and dense

gas ( $T < 500$  K and  $n_{\text{H}} > 1 \text{ cm}^{-3}$ ). We also generate an analogue of observational measures of recent SFRs by calculating the 10 Myr-averaged SFR in the pixels. To do so, we find the mass of all age  $< 10$  Myr star particles in the pixel, and correct for stellar evolutionary effects using STARBURST99 (Leitherer et al. 1999). We choose this time interval because of its approximate correspondence with the time-scales traced by recombination lines like  $\text{H}\alpha$  (Kennicutt & Evans 2012; Velázquez et al. 2020), and to associate ionized gas near  $T \approx 10^4$  K with star-forming regions as a proxy for identifying H II region nebosity (FIRE-2 uses STARBURST99 predictions for the ionizing photon budget of star particles). We also calculate the 40 Myr-averaged SFR in the pixels, for the purposes of associating metallicity scatter with the approximate time-scale of the duration of supernova feedback (and their enrichment).

In comparing with observations, we identify the warm ionized gas column (WIM) and select gas elements with  $|\log T - 4.05| < 1/6$ , regardless of density, as this gas scales with observations of nebular gas; metallicity can typically be measured from metal lines that occur in nebular regions such as [O II], [O III], and [N II] (Asari et al. 2007; Zahid et al. 2012; Andrews & Martini 2013; Boselli et al. 2014; Belfiore et al. 2017; Sánchez, Heckman & Blanc 2017; Toribio San Cipriano et al. 2017; Wang et al. 2019). In our analysis, we associate this gas reservoir with diffuse warm ionized gas haloes surrounding (and to an extent throughout) these galaxies and ‘H II regions’ in star-forming clouds (i.e. pixels where the 10 Myr-averaged star formation rate is non-zero). We compare our ‘H II region’ columns and metallicities ( $Z_{\text{H II}}$ ) with nebular emission observations of, e.g. [O III]. Lastly, we also identify the ‘cold and dense’ gas ( $Z_{\text{CD}}$  throughout), having  $T < 500$  K and  $n_{\text{H}} > 1 \text{ cm}^{-3}$ . We relate this gas in the simulations with that traced by cold dust or CO. We present the total, oxygen and iron gas-phase metallicities throughout our analysis, but focus mostly on the total metallicity of the ‘H II regions,’ and cold and dense gas.

### 3 ANALYSIS AND RESULTS

Fig. 1 shows the evolution of the stellar mass ( $M_{\star}$ ) and 40 Myr-averaged star formation rate ( $\dot{M}_{\star, 40\text{Myr}}$ ) of the five galaxies over the epoch analysed. We rationalize our choice of the 40 Myr-averaged SFR because this quantity traces time-scales where metals are returned to the ISM through core-collapse SNe (Leitherer et al. 2014), and aligns with observations in the UV (Lee et al. 2009). Fig. 1 also includes estimates of quantities for the SMC and LMC, including respective stellar masses  $10^{8.5}M_{\star}$  (Bekki & Stanimirović 2009) and  $10^{9.4}M_{\star}$  (van der Marel et al. 2002), as well as recent star formation rates  $0.3 M_{\odot} \text{ yr}^{-1}$  (Rezaei Kh. et al. 2014; Rubele et al. 2015; Hagen et al. 2017) and  $0.2 M_{\odot} \text{ yr}^{-1}$  (Harris & Zaritsky 2009; Rezaei Kh. et al. 2014), respectively.

Fig. 2 displays the spatial metallicity distribution of the cold and dense gas ( $T < 500$  K,  $n_{\text{H}} > 1 \text{ cm}^{-3}$ ) for a single snapshot around  $t_{\text{lookback}} \sim 0.36$  Gyr for all galaxies in this study with a pixel size of 250 pc. Coloured by their metallicity relative to solar, these maps allow us to characterize the galaxies at a glance in terms of their morphologies, apparent dynamical states, and sizes.

Fig. 3 displays the spatial metallicity distributions of the warm ionized phase (near the  $\text{H}\alpha T \approx 10^4$  K ridge-line) in two of the simulations in this study, **m11e** and **m11h**, in addition to including the before-seen cold and dense gas. We see immediately that the galaxies, as expected, are surrounded by a warm gas halo, and compact star-forming H II regions are spread throughout the galaxy. Below we further discuss the gas-phase metal distributions revealed in these two figures.

### 3.1 Characterizing the individual simulations

We find it important to briefly characterize each simulated galaxy (alphabetically), all originally introduced in El-Badry et al. (2018), with the exception of **m11q** from Hopkins et al. (2018), to appreciate the peculiarities of the metal distributions. For information on the stellar metallicity distributions, we direct the reader to Patel et al. (2022).

An LMC-mass galaxy, **m11d** has a main body of cold and dense gas maintaining a metallicity within  $\pm 0.1$  dex of solar (fairly well-mixed throughout). The galaxy also displays numerous small pockets of metal-rich gas with metallicity  $10^{0.75}Z_{\text{CD}}/Z_{\odot}$ , nearly an order of magnitude larger than the primary body,  $10^{-0.1}Z_{\text{CD}}/Z_{\odot}$ , as a result of repeated feedback events that majorly disturb the gas. Fig. 2 represents **m11d** in a pre-major starburst state ( $t_{\text{lookback}} = 0.36$  Gyr). We observe this large-scale feedback event occurring at  $t_{\text{lookback}} = 0.19$  Gyr, completely disrupting the main body of dense gas. Evident in Fig. 1, **m11d** experiences a significant drop in the star formation rate around the time of the starburst ( $t_{\text{lookback}} = 0.19$  Gyr).

**m11e** displays a prominent main disc around  $\sim 0.5$  solar metallicity, as well as a second, metal-poor (metallicity nearly an order of magnitude below that of the main body) merging galaxy. The imaged snapshot occurs just as the cold and dense components of the satellite and primary body make contact, triggering several smaller feedback/starburst events in the main disc. Prior to merging, we note that each individual galaxy is reasonably well-mixed (within  $\sim 0.1$  dex) in the cold and dense component of the ISM.

Having the largest and most defined disc of the five, **m11h** exhibits an extremely well-mixed body (with a metallicity scatter of  $\pm 0.1$  dex) with few strong feedback events visible in the cold and dense gas. With a mass nearly identical to that of **m11d**, we see from Fig. 1 that **m11h** also has a similar 40 Myr-averaged SFR value up until  $t_{\text{lookback}} = 0.2$  Gyr, though it remains much more stable than **m11d**, largely due to the lack of disruptive feedback taking place. A slight metallicity gradient is visible (see Fig. 5 for a quantitative presentation of the metallicity gradient, and Fig. A1 to see the metallicity relative to galactic average).

One of the smaller FIRE-2 dwarf galaxies in this analysis, **m11i** is around three times the mass of the SMC and exhibits several ‘small’ feedback events. This is evident in the snapshot pictured in Fig. 2 as the cold and dense gas body of the galaxy is minorly disrupted. These starbursts remain infrequent, and this galaxy is similarly well-mixed like the three previously described.

The lowest-mass, and physically smallest, galaxy in this study is **m11q** at just below twice the SMC mass. While similar to **m11i**, it has a metallicity lower by  $\sim 0.3$  dex. We note that this galaxy’s metallicity is nearly identical to that of the merging body in **m11e**, and is also strikingly well-mixed.

#### 3.1.1 Maps of H II<sub>Z</sub> versus CD<sub>Z</sub>

While we see most of the characteristics (such as discs) of our galaxies in the cold and dense gas component, it is important to analyse other components of the ISM, as the cold molecular gas is more difficult to detect (Krčo et al. 2008; Boselli et al. 2014; Querejeta et al. 2019); more observable phases (such as the ‘H II regions’) may provide insight into how to interpret properties of the cold and dense gas phase. To provide a diverse example of these varying components, Fig. 3 displays two galaxies, **m11e** and **m11h**, in the three ISM components that we study in this paper: from left to right, we depict the H II gas (with diffuse component), nebular

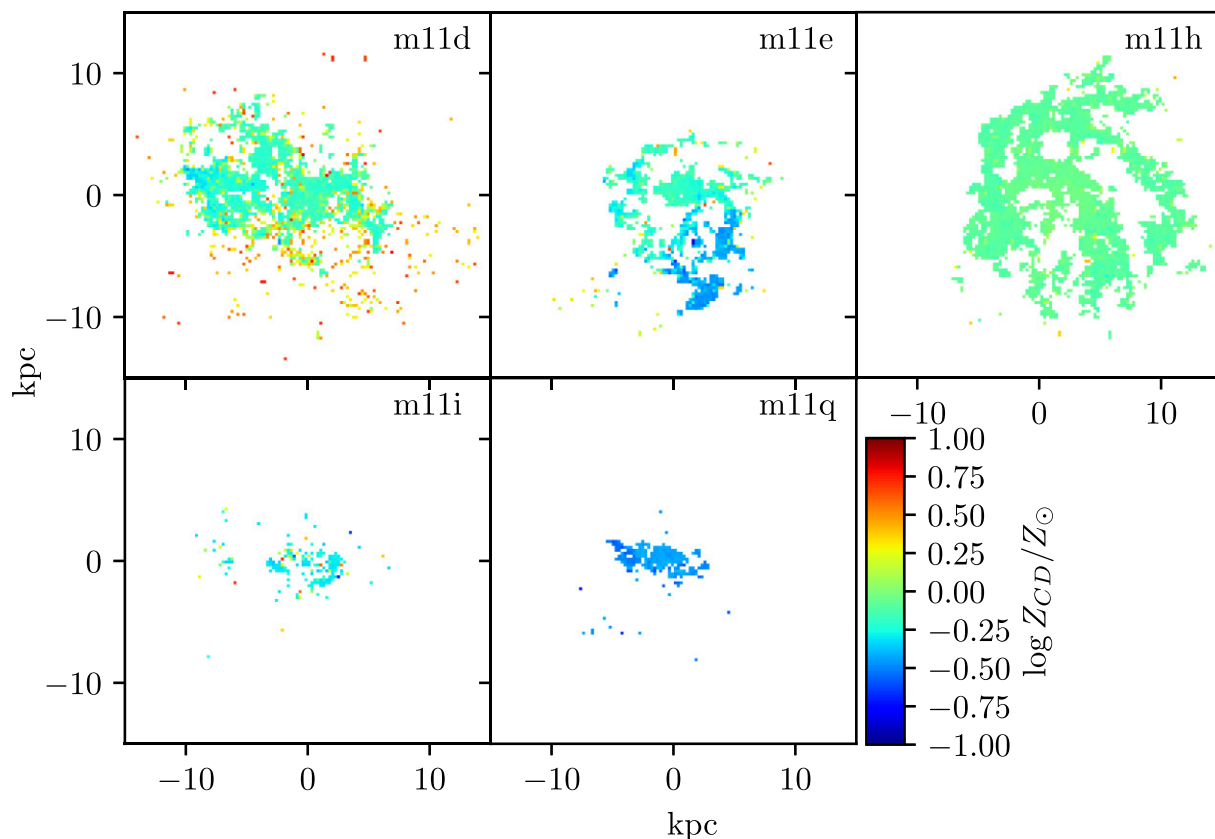


**Figure 2.** Spatial distributions of metallicity of cold and dense gas component ( $T < 500$  K) of FIRE-2 galaxies with a pixel size of 250 pc at a single snapshot,  $t_{\text{lookback}} \approx 0.36$  Gyr, coloured by their metallicity relative to solar. *Upper-left:* galaxy **m11d** pre-starburst; LMC-mass galaxy that exhibits a majorly disrupted gas disc that is constantly expanding after multiple starbursts. Disc is well-mixed with regions of high enrichment. *Top-centre:* galaxy **m11e**; main disc is well-mixed at  $\log Z/Z_{\odot} \approx -0.25$  and exhibits an infalling satellite galaxy with a much lower metallicity ( $\log Z/Z_{\odot} \approx -0.5$ ). The galaxies have not yet fully merged, with the satellite now near its first periastris. *Upper-right:* galaxy **m11h**; LMC-mass small spiral galaxy with a well-mixed disc and a slight metallicity gradient. *Lower-left:* galaxy **m11i**; small galaxy near three times the SMC mass with a disrupted gas disc from a recent starburst that is still relatively well-mixed. Metallicity is comparable to the main disc of **m11e**. *Bottom-centre:* galaxy **m11q**; another small galaxy just under twice the SMC mass undisturbed by starbursts or recent star formation.

regions (H II gas with cospatial 10 Myr-averaged SFR), and cold and dense gas (previously described in Fig. 2).

In the case of **m11e**, we can clearly see the warm ionized gas inflow from the merger being mixed into the main disc, including how the main galaxy and the infalling companion are nearly homogeneous in their independent distributions ( $\pm 0.1$  dex) in both Figs 2 and 3. It is also evident that the ionized gas extends across a larger region than the cold and dense gas, and so the ionized gas between the two galaxies begins interacting far before the cold and dense gas counterpart. Here, we also note the inflow in both ISM components appears to be of much lower metallicity than the main body.

Similar comments can be made about **m11h** despite its absence of a merger. The ionized gas component extends beyond the cold and dense gas, and exhibits a similar metallicity gradient. We can see evidence of metal-poor inflows on the outskirts of the ionized gas and small areas of higher metallicity spread throughout.

Upon examination of the nebular regions in both galaxies in Fig. 3, we see that they are a clear tracer of the cold and dense gas, despite the differences between the spatial distributions of the two. This finding is particularly significant, since the regions of ionized gas with recent star formation ( $< 10$  Myr-averaged) may be able to provide an accurate estimate of the metallicity of the cold and dense

gas component. We include versions of Figs 2 and 3 in Appendix A where we have scaled the colourbar to the average metallicity in each galaxy to show the internal variations more clearly.

### 3.2 Mass–metallicity Relation (MZR)

After exploring the spatial metallicity distributions of our selection, we investigate the correlation between gas-phase metallicity and stellar mass (MZR) in the range of masses,  $M_{\star} \sim 10^{8.75} - 10^{9.75} M_{\odot}$ , in this study. Fig. 4 displays the gas-phase MZR in our selection of galaxies, averaged over all of the pixels from each snapshot, in both the cold and dense gas and the nebular regions ( $T \approx 10^4$  K with 10 Myr-averaged star formation) for the total metallicity in solar units, O in  $12 + \log(\text{O}/\text{H})$  units, and Fe in  $12 + \log(\text{Fe}/\text{H})$  units, the latter of which is not typically observed in the gas-phase. The data from each simulation are plotted against observations from Sánchez et al. (2019) and Tremonti et al. (2004) in  $12 + \log(\text{O}/\text{H})$ , which we scale to the appropriate units for the top panel. We also include values for the SMC and LMC mean gas-phase metallicities from Pagel et al. (1978) and masses from Bekki & Stanimirović (2009) and van der Marel et al. (2002). Observational values of the MZR can vary in terms of the zero-point and slope depending on the adopted calibration, whereas the theoretical MZR here can depend

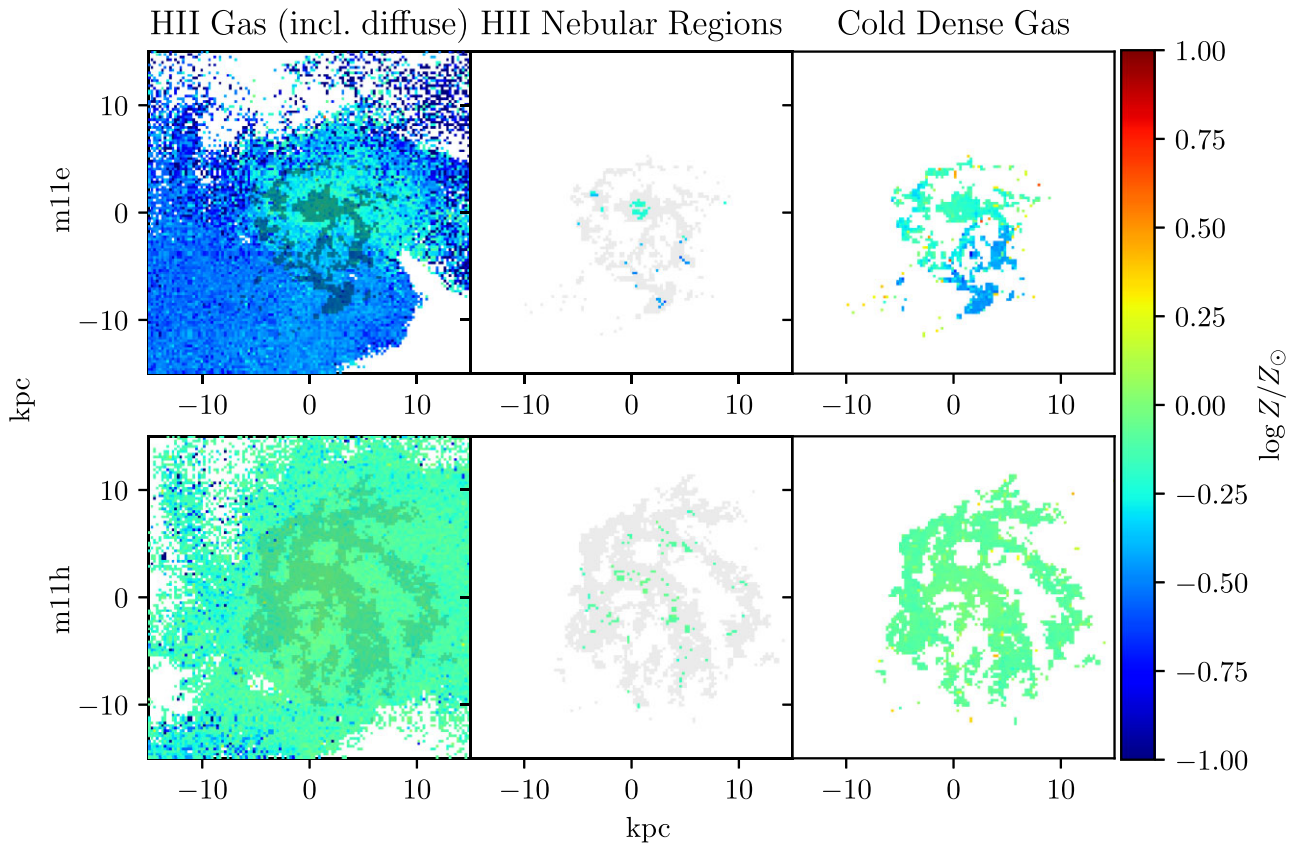


**Figure 3.** Metallicity distributions in various ISM components at 250 pc pixel size for two of the galaxies in this paper (**m11e** and **m11h**) from a single snapshot at  $t_{\text{lookback}} \approx 0.36$  Gyr, coloured as Fig. 2. *Left column:* Hydrogen gas with  $T \approx 10^4$  K (including diffuse ionized component). Top-left panel exhibits **m11e**'s main body at a slightly higher metallicity envelope and the infalling companion. As the companion merges, the ionized gas halo is mixing into the main body. Bottom-left showcases the well-mixed hydrogen of **m11h** with a weak apparent gradient and some metal-poor gas mixing in the outskirts ( $R \geq 10$  kpc). *Middle column:* H II nebular regions ( $T \approx 10^4$  K with 10 Myr-averaged star formation). Centre-top panel shows a small distribution of gas in **m11e** with nebular regions tracing part of the infalling companion, and the centre of the main body. Centre-bottom shows how nebular emission tracks star-forming regions, closely tracing the dense gas peaks in **m11h**'s spiral arm structure. *Right column:* Cold and dense gas ( $T < 500$  K) metallicity as shown in Fig. 2, shown for comparison with diffuse H II gas and nebular regions.

on quantities such as the adopted nucleosynthesis prescriptions, discussed in Section 2 (Tremonti et al. 2004; Finlator & Davé 2008; Kewley & Ellison 2008; Maiolino et al. 2008; Calura et al. 2009; Maier et al. 2015; Ma et al. 2016, 2017; Maiolino & Mannucci 2019; Sánchez et al. 2019; Spitoni et al. 2020). Therefore, it can be expected that there will be some offset when comparing the simulated and observed MZR.

Most of the FIRE-2 dwarf galaxies that we analyse in this paper appear to match the observed MZR, with galaxies **m11d**, **m11h**, and **m11i** most closely following the observational distributions. **m11h** appears to fall just above the upper limit of observations from Sánchez et al. (2019). While **m11e** and **m11q** still fall within the range of observations, both exhibit a decreasing relationship of metallicity with stellar mass in Fig. 4 resulting in contrast to **m11d**, **m11h**, and **m11i**.

We can also combine measurements of stellar mass (van der Marel et al. 2002; Bekki & Stanimirović 2009) and metallicity to use Fig. 4 to compare the simulations and MCs. Metallicity values for the SMC and LMC are taken to be  $0.2 Z/Z_{\odot}$  and  $0.5 Z/Z_{\odot}$ , respectively, values from Russell & Dopita (1992) and more recently confirmed by Roman-Duval et al. (2019). For  $12 + \log(\text{O}/\text{H})$ , we use values of 7.98 and 8.39, respectively (Pagel et al. 1978). While different measurements of the abundance of oxygen exist, we utilize

the values for each MC from Pagel et al. (1978) for consistency. We are confident that these values are accurate as they remain extremely similar to other derived values for both the SMC (8.03–8.41, Toribio San Cipriano et al. 2017) and LMC (8.35–8.55, Toribio San Cipriano et al. 2017).

Most of the galaxies in our sample (**m11d**, **m11h**, and **m11i**) are in good agreement with results found in other literature using FIRE to evaluate the MZR, including Ma et al. (2016) and Escala et al. (2018), the former of which also compares the MZR in FIRE-1 galaxies with observational data from Tremonti et al. (2004) at  $z \approx 0$ .

There appears to be little difference between the two plotted ISM phases. One difference is that the warm ionized gas with recent star formation appears to have higher scatter in the 5–95 per cent range of the distribution (thin errorbars in Fig. 4), while the cold and dense gas displays less variation. Average metallicity appears to be identical between the ISM phases with the exception of **m11q** and the final few snapshots of **m11d**, which exhibit a lower metallicity in the nebular regions than the cold and dense gas.

We note that **m11e**'s metallicity experiences a sharp drop in the short time-span of two snapshots, beginning at about  $t_{\text{lookback}} = 0.60$  Gyr and lasting approximately 50 Myr. This is a rapid time-frame for a drop in metallicity of half a magnitude, and can be attributed to the major-merger at that time, as they are known to

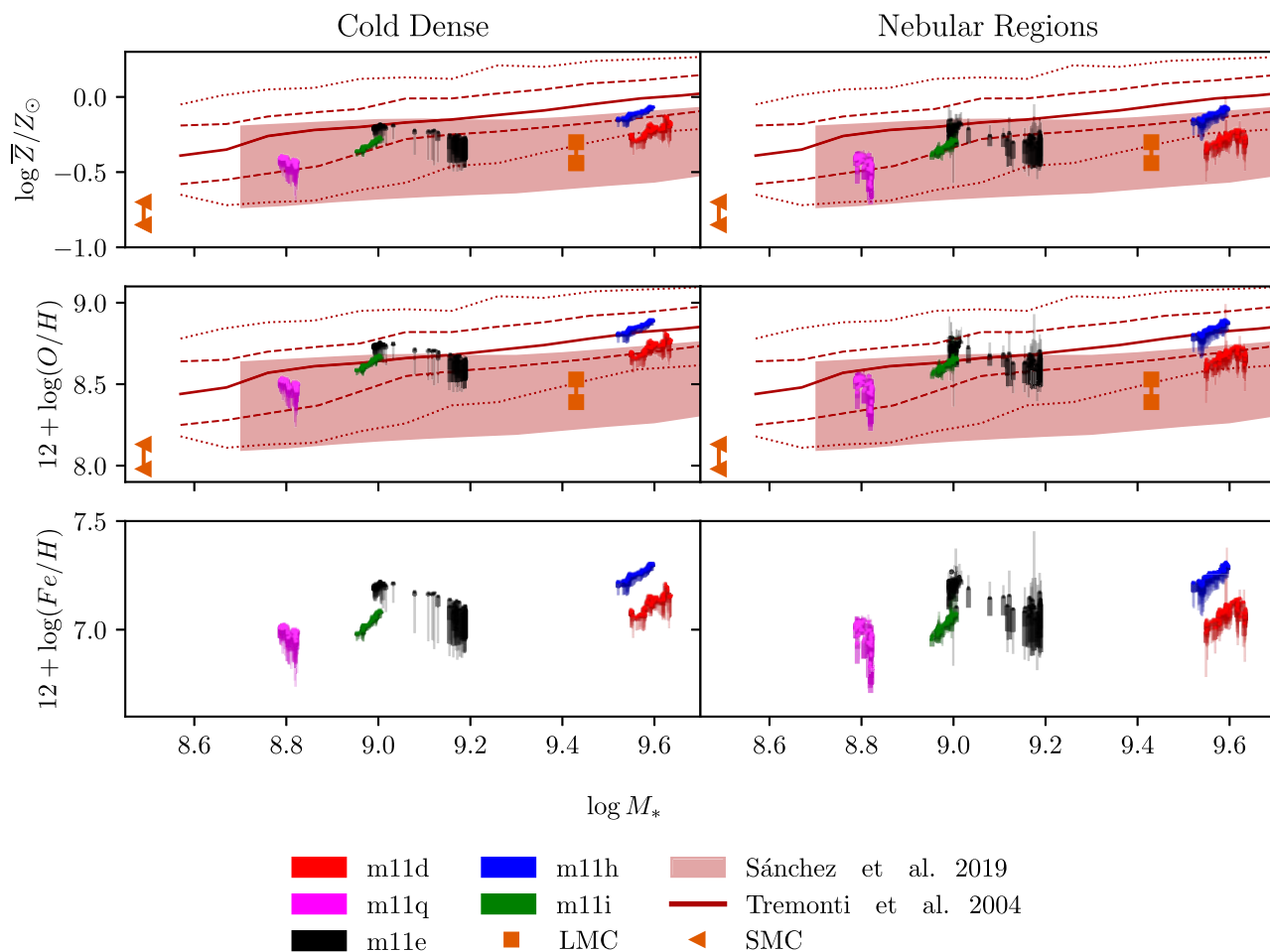


**Figure 4.** Gas-phase mass–metallicity relation (MZR) plots of five FIRE-2 dwarf galaxies over the analysis period ( $t_{\text{lookback}} = 1.4 - 0$  Gyr,  $0 < z < 0.11$ ), in cold and dense gas ( $T < 500$  K) and H II gas ( $T \approx 10^4$  K with recent SFR), in total metallicity (top row), O (centre row), and Fe (bottom row). Each point represents different snapshots, denoting the average metallicity and stellar mass of all the designated ISM component gas in each, with colours as Fig. 1. Thick bars denote 25–75 per cent range of distribution of 250-pc pixels within each snapshot and thin bars represent 5–95 per cent range. Orange facing-left triangles represent SMC metallicities (Pagel et al. 1978; Russell & Dopita 1992) and mass (Bekki & Stanimirović 2009), and orange squares represent LMC metallicities (Pagel et al. 1978; Russell & Dopita 1992), and mass (van der Marel et al. 2002). Shaded red regions represent the range of observational data from Sánchez et al. (2019). Dark red lines show observational data from Tremonti et al. (2004), with the solid line showing the median data points, the dashed lines showing  $\pm 1\sigma$ , and dotted lines as  $\pm 2\sigma$ . There seems to be little difference between cold dense and nebular regions, with nebular regions exhibiting scatter to slightly higher abundances in the tails of the distributions. Simulations are generally in agreement with estimated range of metallicities from Tremonti et al. (2004) and Sánchez et al. (2019).

cause such dramatic drops in gas-phase metallicity (Kewley, Geller & Barton 2006; Reichard et al. 2009; Ellison et al. 2013; Hopkins et al. 2013; Cortijo-Ferrero et al. 2017).

**m11q**, however, has no such apparent merger in our analyzed time-frame to explain such a significant drop in metallicity, and we see that this occurs throughout the entire span of the  $\sim 1.4$  Gyr analysed. Instead, this galaxy appears to be undergoing significant accretion of metal-poor gas on to its outskirts, explaining the steep negative evolution in metallicity (and its steep metallicity profile seen in Fig. 5).

We also note that each galaxy appears to have variations both within themselves at a certain time (a single point in Fig. 4) and over time. For example, galaxies such as **m11d**, **m11h**, and **m11i** appear to be primarily consistent with their evolution, with **m11d** exhibiting more dependence on the scatter caused by major starbursts at later times. We can see that **m11e**'s metallicity slowly begins increasing over time and with stellar mass in the system, following what we might expect from the MZR, but only before the merger

appears at  $t_{\text{lookback}} = 0.60$  Gyr. Galaxy **m11q** clearly has a distribution opposite that of the remaining galaxies; the average metallicity does not increase over this time. Instead, due to accretion (discussed later in Section 3.4), the metallicity decreases.

### 3.3 Metallicity profiles

We plot radial metallicity profiles of the FIRE-2 dwarf galaxies in the cold and dense gas in Fig. 5. Typically, we would expect very slight negative relationships in the radial profile for dwarf galaxies, if they exist at all. Ma et al. (2017) notes that galaxies with strong perturbations usually have flatter gradients. Turbulence driven at least in part by feedback mixes the metals, leading to distributions with a more uniform metallicity.

Furthermore, feedback shapes metallicity gradients because star formation is clusted. As a result, this clustered feedback disrupts the gas in concentrated regions. More massive galaxies with extended discs and smooth SFRs will have negative gradients as they become

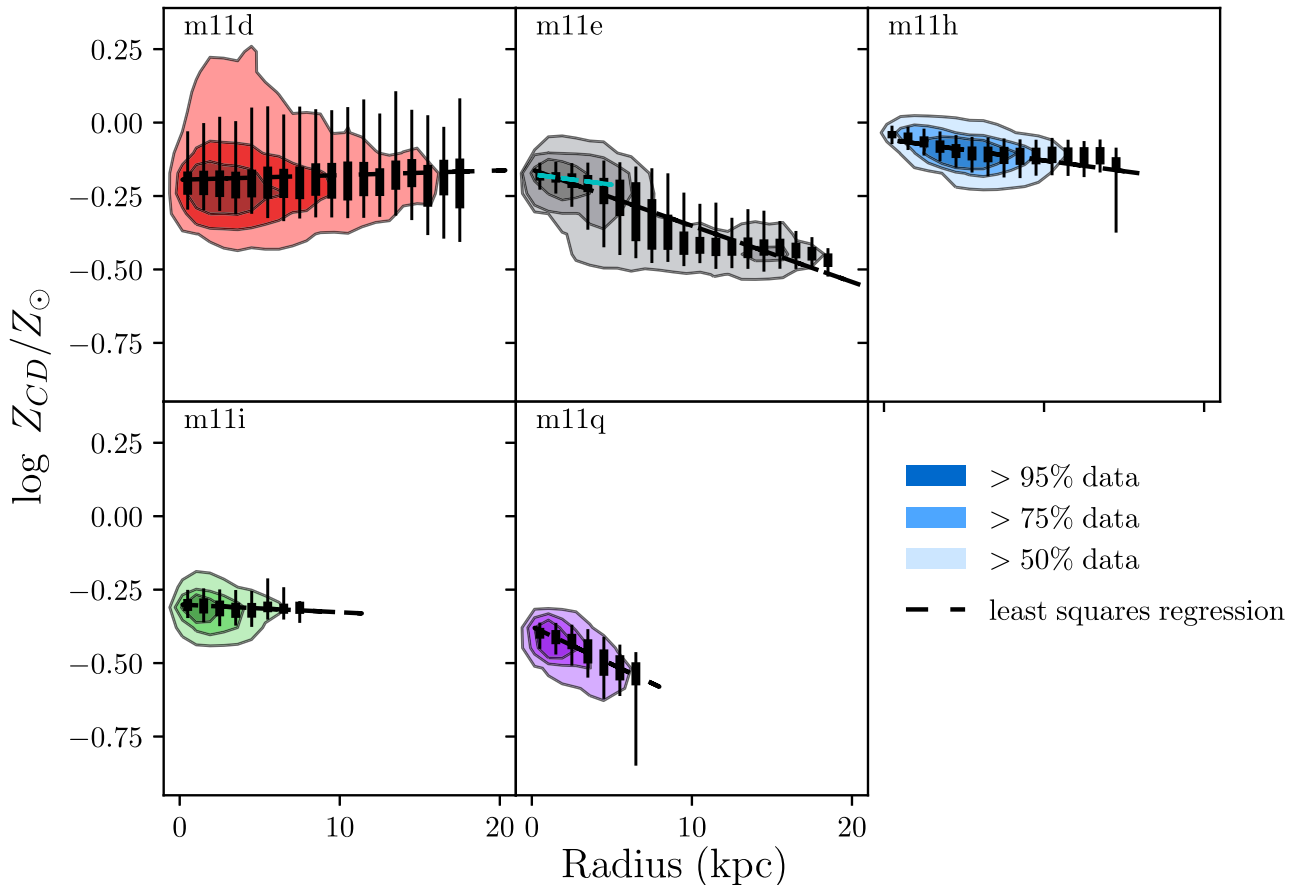


**Figure 5.** Radial profiles of the cold and dense gas metallicity in all five galaxies, analysed here with 250 pc pixel size, where each distribution contains all pixels of the corresponding galaxy (across all snapshots, for  $t_{\text{lookback}} = 1.4 - 0$  Gyr,  $0 < z < 0.11$ ). Shaded regions represent 50, 75, and 95 per cent of data. Colours are as Fig. 1, with box and whiskers representing the same ranges as Fig. 4 in each radial bin. The least-squares regression, denoted by the dashed black line, is fit through the entire distribution with the exception of **m11e**, where an additional cyan line has been plotted through only the main galaxy body before the satellite appears in the simulation ( $R \geq 5$  kpc and  $t_{\text{lookback}} > 0.6$  Gyr). *Upper-left: m11d*; The galaxy is majorly disrupted due to starbursts, producing a positive metallicity gradient. *Center-top: m11e*; An apparent steep metallicity gradient appears due to the merging companion. See cyan line for more accurate fit of main galaxy body (and further discussion in Section 3.5). *Upper-right: m11h*; An LMC-mass spiral with inside-out growth; slight negative metallicity gradient consistent with inside-out disc growth models. *Lower-left: m11i*; Flat to slight gradient owing to a very well-mixed nature. *Centre-bottom: m11q*; A very steep gradient possibly due to metal-poor inflows that significantly affect the galaxy due to its small size and mass.

less disrupted by individual star formation events, as supported by Bellardini et al. (2021). Dwarf galaxies, which are inherently more susceptible to feedback due to their small nature, are dominated by perturbations and exhibit extremely weak (if not flat) gradients (El-Badry et al. 2016; Mercado et al. 2021).

However, of the galaxies in this study, not all follow these expectations, and we therefore find it necessary to iterate through the idiosyncrasies of the radial gradient of each galaxy.

**m11d** is the only galaxy in our selected sample that appears to exhibit a positive gradient, although it is slight. This galaxy also exhibits the largest spread in metallicity, covering just more than an order of magnitude. This galaxy undergoes several significant large-scale starburst/feedback episodes, the most of any galaxy studied here, so we consider this as a possible cause behind the positive gradient.

**m11e** is a particularly interesting case in terms of the metallicity profile. The merging body is clearly visible as a second distribution, and the significant drop in metallicity creates a particularly steep gradient. Because we recognize that the major-merger is the cause of this unique gradient, we chose to fit a line through the main body of **m11e** by limiting the radius to only the primary disc, and selecting

to fit the corresponding line to snapshots where the satellite galaxy is not present in the cold and dense gas. As a result, we believe we obtain a far more realistic value for **m11e**'s metallicity gradient in the cold and dense gas before the merger is present, represented by the dashed cyan line, and we are therefore able to analyse the galaxy's gradient both pre-merger and during the merger, matching findings by Hopkins et al. (2013). We note here that our analysis time-frame concludes before the two bodies are able to effectively fully mix, which is why the gradient appears to be particularly steep. Once the galaxies in **m11e** merge at a later time than this study covers, we predict that the gas reservoirs will mix fully into one distribution, resulting in a less steep metallicity gradient but an overall lower average  $Z$ . We explicitly note that the steepness of **m11e**'s gradient here is because both gas reservoirs have *just* begun mixing.

While it maintains a metallicity slightly higher than that of the pre-merger **m11e**, the body of **m11h** has a nearly identical metallicity gradient as the main body of **m11e**. Here, we see a smaller distribution than in the previous two galaxies, both in terms of size and spread. While this galaxy is smaller, this negative gradient matches what is expected for inside-out galaxy formation in disc galaxies of higher masses, both in observations (Magrini et al. 2016; Sharda et al. 2021)

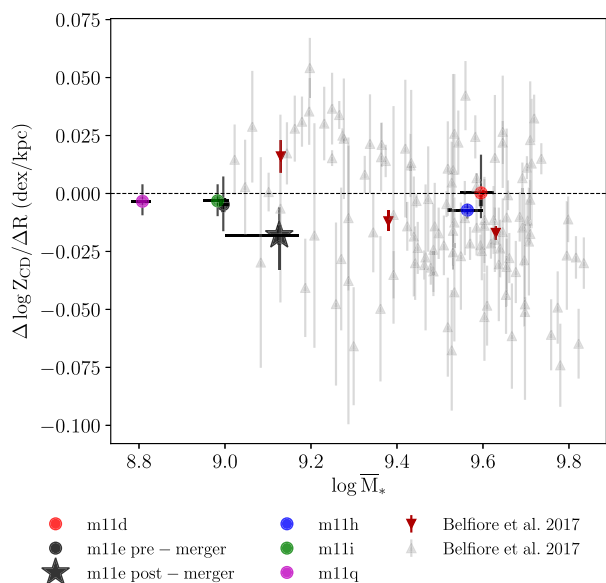


**Figure 6.** Cold and dense gas metallicity gradients as a function of stellar mass (MZGR) for all FIRE-2 dwarfs, averaged over the entire analysis period ( $t_{\text{lookback}} = 1.4 - 0$  Gyr,  $0 < z < 0.11$ ), with **m11e** being split into pre-merger (circle) and post-merger (star). Points denote the position of the galaxy’s average stellar mass and average slope of metallicity gradient in dex per kpc (displayed in Fig. 5). Thick vertical bars denote 25–75 per cent of data within that interval and thin vertical bars represent 5–95 per cent of data. Thick horizontal bars represent the change in stellar mass, with the leftmost point being the first snapshot and the rightmost point depicting the last snapshot. Colours are as Fig. 1. Grey and burgundy points and errorbars are observational data in the MaNGA survey from Belfiore et al. (2017), where grey points are individual galaxies and red points are the median values of 0.25 dex stellar mass bins. Galaxies have weak to negative gradients; they exhibit a positive slope shortly after starbursts, as in the case of **m11d**. **m11e** clearly has a gradient similar to that of **m11h** and **m11i** until the merger. Simulations are consistent with observations.

and simulations (Pilkington et al. 2012; Ma et al. 2017; Bellardini et al. 2021).

As seen in Fig. 2, **m11i** is our smallest galaxy in the sample and displays the least scatter in its metallicity profile. A large majority of the gas is concentrated within 5 kpc and the metallicity stays within approximately 0.25 dex. This is the flattest gradient of our sample, and displays an extremely slight negative trend.

**m11q** is similar to both **m11h** and **m11i** in terms of having little spread in metallicity over most of the galaxy, but it has a strong negative gradient. This gradient in particular is similar to that found in **m11e** post-merger, but there is no major-merger in this time-frame to explain such a stunningly steep gradient. In this case, we attribute this steep gradient to a high rate of metal-poor gas accretion in the galactic outskirts. The cold and dense gas reservoir appears to increase by just over  $10^7 M_{\odot}$  over 200 Myr (initially about  $10^{8.8} M_{\odot}$ ), a significant mass increase over such a time-span, and corresponds to the period where **m11q**’s variations in metallicity are at their highest.

Similar gradients can be found in other literature on FIRE galaxies, such as in Ma et al. (2017), despite the fact that they use high-redshift and higher mass galaxies.

### 3.3.1 Mass–metallicity gradient relation (MZGR)

We compare the MZGR in these simulations to that of data from the SDSS MaNGA Survey in Belfiore et al. (2017), referenced in Fig. 6.

However, we note that these observations are complete for stellar masses greater than  $10^9 M_{\odot}$ , and not all of our analysed galaxies fall within this range. We plot all galaxies studied on this figure, splitting **m11e** into pre and post-merger in order to more accurately compare the galaxy’s ‘true’ gradient with and without the presence of the merging companion. For the galaxies that overlap with the mass range in Belfiore et al. (2017), we see that the simulations are consistent with observations. While the scatter in individual galaxies of the observations appears to be far greater than our simulations, the median observational values (burgundy inverted triangles of Fig. 6) are still consistent with our results, and we note the small-number statistics of having only 5 galaxies in our sample.

Most gradients are flat or extremely close to zero, with **m11d** exhibiting a slightly positive scatter, despite having the same stellar mass as **m11h**. In addition, **m11h** exhibits the least amount of variation of its gradient. The three galaxies **m11e** (pre-merger), **m11i**, and **m11q** all have a roughly identical gradient, despite **m11q**’s smaller stellar mass. We also make note of the significant drop in metallicity and increase in stellar mass for the separately distinguished post-merger phase of **m11e** shown in Fig. 6.

We include a version of Figs 5 and 6 using nebular gas metallicity in Appendix B. The results are qualitatively similar, reassuring for our comparison with observations.

### 3.4 Enrichment variation between ISM phases

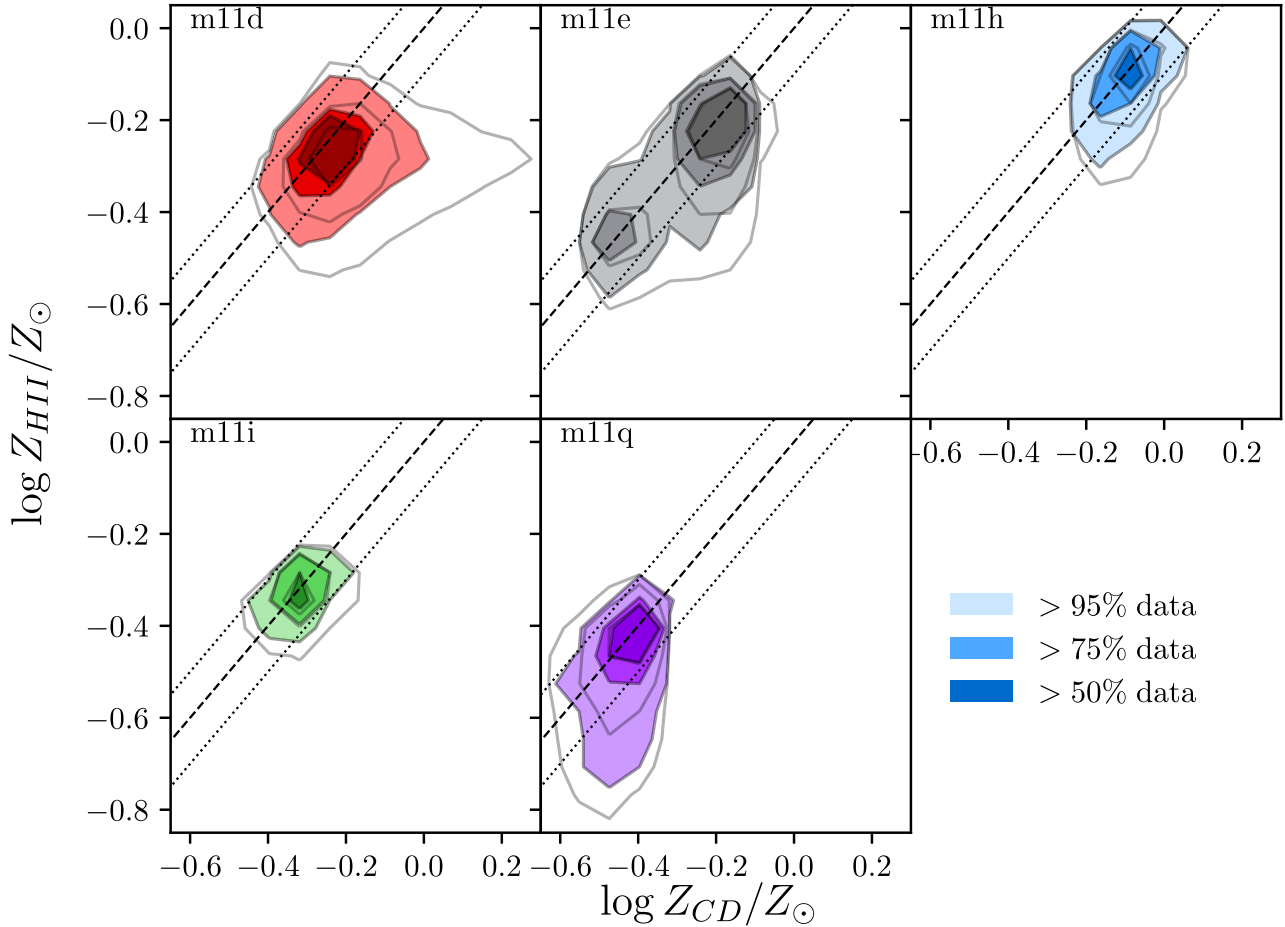
Studying the relative metallicity enrichment between various phases of the ISM, such as the cold and dense gas and ionized gas, allows us to gain understanding as to whether the metals are moving spatially or between phases. All galaxies studied here appear to have a tight correlation in relative enrichment between the cold and dense and nebular ISM phases, with scatter remaining of approximately  $\pm 0.1$  dex.

Fig. 7 provides an overview of the metallicity enrichment between the cold and dense gas and ionized gas. Remarkably, there is no significant bias in the average enrichment of phases in any of the galaxies. This occurs for both the diffuse and nebular H II (filled and unfilled contours in the figure), although we see slightly more scatter in the diffuse gas, which is consistent with other FIRE simulations at larger masses, such as MW-mass galaxies in Bellardini et al. (2021). This finding is significant because we may have expected a bias in the nebular regions relative to the cold and dense gas; nebular regions here are in the immediate vicinity of stars that are actively enriching the gas, as they are defined to have non-zero 10 Myr-averaged star formation. The cold and dense gas does not have a similar requirement. We reiterate: the metallicity of nebular regions appears to closely trace the metallicity of the cold and dense gas component.

The two distributions in metallicity of **m11e** are particularly noticeable. This brings to attention that throughout **m11e**’s merging process with its satellite galaxy, the two ISM phases of the merger *still* primarily stay within  $\pm 0.1$  dex of each other.

Also evident is **m11q**’s steep metallicity scatter to low  $Z$  in the nebular ISM. Again, this is a rather interesting result since **m11q** is one of the smallest galaxies in the sample, and it appears to exhibit as much (if not more) scatter as **m11d**, which has significantly more feedback occurring on a much larger scale in relation to the size of the galaxy.

Fig. 8 contains data from every pixel of the simulations, showing the relative enrichment between metallicity in the cold and dense gas, and H II regions. While we already know from the contours that most of the data are concentrated within the  $\pm 0.1$  dex lines, we note that the extreme outliers take on a very specific shape:



**Figure 7.** Comparing the enrichment of the cold and dense gas and H II gas (nebular and nebular + diffuse regions) in the five galaxies at 250 pc pixel scale for all snapshots over the analysed period ( $t_{\text{lookback}} = 1.4 - 0$  Gyr,  $0 < z < 0.11$ ). Filled contours denote 50, 75, and 95 per cent of data inclusion in nebular regions; unfilled contours represent all of the H II gas (nebular + diffuse regions). Dashed line denotes equal abundances in the two phases, and dotted lines represent  $\pm 0.1$  dex enrichment. Colours are as Fig. 1. In all cases, observable (nebular) regions and cold and dense gas are close to equal in metallicity (with about  $\pm 0.1$  dex scatter). Despite larger starbursts, **m11d** is mixed fairly well, though it appears to be skewed in the higher  $Z_{\text{CD}}$ -direction. **m11e** has a well-mixed distribution, but two clear groupings are visible between the galaxy and a companion. **m11h** and **m11i** are both very well-mixed with no significant departures and little difference between nebular and diffuse H II. **m11q** has a spray to low H II enrichment relative to the cold dense component, but is still relatively well-mixed.

this scatter is either completely horizontal, with no slope, or the slope is completely vertical. Most of the points making up this scatter appear to have low surface density in the cold and dense gas ( $< 3M_{\odot}\text{pc}^{-2}$ ), but their presence and peculiar slopes merits further investigation.

In order to understand the outliers of  $Z_{\text{CD}} = Z_{\text{HII}}, \pm 0.1$  dex, we identified one region of outliers for each galaxy in Fig. 8. For example, in **m11d**, we investigated higher  $Z_{\text{CD}}$  enrichment relative to  $Z_{\text{HII}}$  (red-dashed rectangle.) In the other four galaxies, we investigated lower  $Z_{\text{HII}}$  enrichment relative to  $Z_{\text{CD}}$  (black, blue, green, and magenta, respectively). We then made maps of pixels in these identified regions (smaller panels of Fig. 8, similar to Figs 2 and 3) to glean information on the physical processes occurring in these areas of the galaxy.

There is a clear connection in what seems to be causing the directional slopes of outliers. From the inset maps, we generally conclude here that  $Z_{\text{CD}}$  enriched more than 0.1 dex of  $Z_{\text{CD}} = Z_{\text{HII}}$  is caused by metal-rich starbursts, and a more-enriched  $Z_{\text{HII}}$  is caused by metal-poor inflows into the galaxy.

This information from the relative ISM gas-phase metallicities follows what we see in the behaviour of each galaxy from Section 3.1:

Galaxies that are dominated by feedback/starbursts, such as **m11d** (and **m11i** to a small extent), will experience a largely flat gradient. The slope may be slightly negative if the galaxy is smaller, as in the case of **m11i**, or slightly positive if the galaxy is larger, as in the case of **m11d**. On the other hand, reaching back to the peculiar case of **m11q**, it can easily be seen how the metallicity profile is influenced by inflows/accretion. **m11q** is both the smallest galaxy in the sample and appears to have a large amount of extremely metal-poor gas accretion. This can directly explain the results of Fig. 5, and why the gradient of **m11q** is far more influenced by this accretion.

### 3.5 Merging metallicity distributions

**m11e** is unique in that it has a clear major merger during the  $t \sim 1.4$  Gyr studied. We find it important to further analyse the effect of the merger on the primary galaxy in terms of metallicity enrichment patterns.

Fig. 9 shows the merger in the cold and dense gas, from roughly the time the companion appears in our analysis ( $t_{\text{lookback}} = 0.76$  Gyr) to the end of the analysed period ( $t_{\text{lookback}} = 0$  Gyr). We see that the infalling galaxy appears to be roughly the same size as the main body,

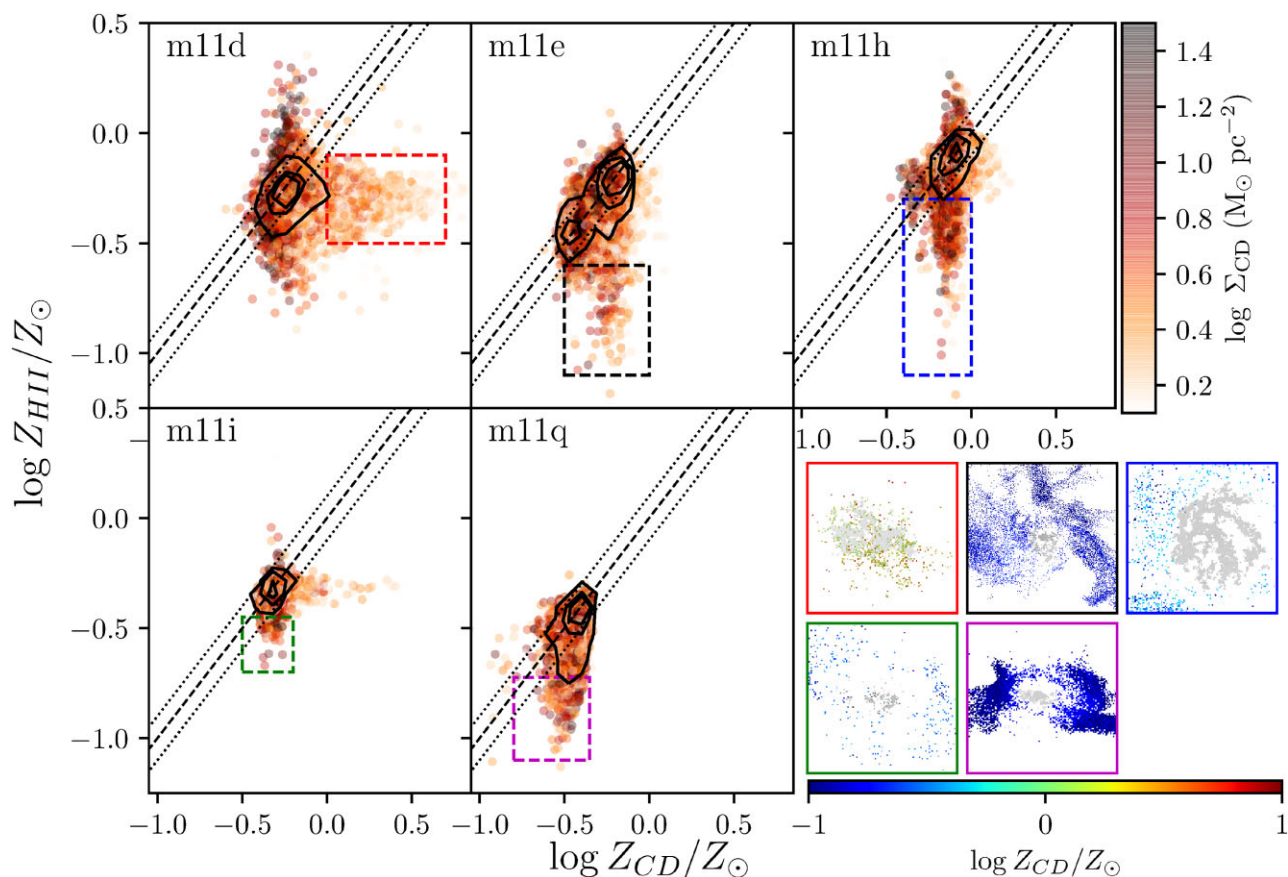


**Figure 8.** *Main panels:* Comparison of cold and dense gas abundances to H II gas abundances from all snapshots for each galaxy over the entire analysed period ( $t_{\text{lookback}} = 1.4 - 0$  Gyr,  $0 < z < 0.11$ ). Points are representative of every 250 pc square pixel, including diffuse H II gas, and are colour-coded with the cold dense gas surface density ( $M_{\odot} \text{pc}^{-2}$ ). Unfilled contours denote 50, 75, and 95 per cent of data inclusion in nebular regions. Dashed and dotted lines are as Fig. 7. Dashed rectangles, with colours as Fig. 1, represent areas of scatter from the one-to-one line that we selected to further study. *Smaller inset panels:* In the lower right corner, the colour-coordinated image for each galaxy (ordered as larger panels) shows the spatial distribution of the boxed scatter in the larger five panels, highlighting their physical origin in the snapshot occurring at  $t_{\text{lookback}} = 0.36$  Gyr. The full  $Z_{\text{CD}}$  distribution in grey, similar to those shown in Fig. 3. **m11d**'s imaged scatter in the red panel, where  $Z_{\text{CD}}/Z_{\odot} > 0$ , clearly demonstrates that scatter in the higher  $Z_{\text{CD}}$ -direction is resultant of metal-rich starbursts. The analysed scatter for **m11e**, **m11h**, **m11i**, and **m11q** all show metal-poor H II gas falling into the galaxies, and in cases like **m11q**, these inflows contribute to a particularly steep metallicity gradient.

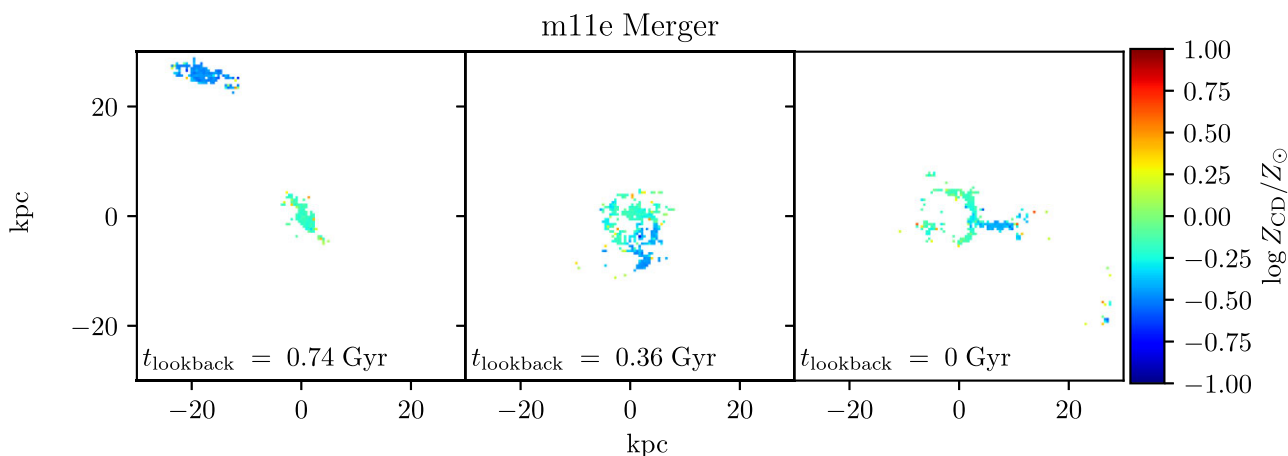


**Figure 9.** Spatial distributions of cold and dense gas ( $T < 500$  K) of **m11e** with a pixel size of 250 pc in three snapshots ( $t_{\text{lookback}} \approx 0.76, 0.36,$  and  $0$  Gyr, respectively), colored as Fig. 2. *Left:* One of the first appearances of the merging companion galaxy in our analysis. On first infall, the cold components have not yet mixed. *Centre:* Companion galaxy is close to pericentre, and the cold components have begun to mix. *Right:* Merging galaxy causes a significant starburst in the main disc of **m11e**, producing a shape similar to the Mice and Antennae galaxies.

but with a metallicity that is nearly half a dex lower. Both galaxies appear to have their metallicity nearly uniformly distributed in the cold and dense gas.

As we see time pass and the satellite spirals into the main body, the cold and dense components appear to first make contact and complete the first periastris around  $t_{\text{lookback}} \sim 0.36$  Gyr, the second panel of Fig. 9. The cold and dense phases of the two galaxies continue to swirl and interact, setting off minor starbursts, before finally setting off a major starburst that disrupts the entirety of **m11e**'s main body in the last snapshot ( $t_{\text{lookback}} = 0$  Gyr), producing an interesting shape reminiscent of the Mice interacting galaxies (NGC 4676; Read 2003; Barnes 2004), or the Antennae galaxies (NGC 4038/NGC 4039; Karl et al. 2010; Lahen et al. 2018; Bemis & Wilson 2019; Tsuge et al. 2021). Over this same analysis period, we can see the satellite very slightly increase in its overall metallicity.

While previous literature such as Torrey et al. (2012) indicates that major mergers in disc galaxies typically flatten the metallicity gradient through metal-poor inflows, we would like to note that the merging of **m11e**, as a dwarf galaxy, requires a unique perspective. Representative through Figs 5, 6, and 9, the apparent gradient of **m11e** steepens. Therefore, the analysis of major mergers between larger disc galaxies and dwarf galaxies, like **m11e**, may need to take into account the mixing time-scales and the stage of the merger. In this case, the main galaxy of **m11e** and its merging companion have not been interacting long enough to fully mix their gas reservoirs. Therefore, since literature strongly supports that merging companion galaxies lower the overall system metallicity, **m11e**'s metallicity will overall decrease once both galaxies are fully mixed, but likely not to the extent that we see in Fig. 5 (Kewley et al. 2006; Ellison et al. 2008; Michel-Dansac et al. 2008; Reichard et al. 2009; Ellison et al. 2013; Hopkins et al. 2013; Torres-Flores et al. 2015; Benítez-Llambay et al. 2016; Cortijo-Ferrero et al. 2017; Maiolino & Mannucci 2019).

We are equally interested in the metallicity as a function of time, therefore further analysing the distributions of metallicity in both galaxies through both the nebular regions (HII with recent star formation) and the cold and dense gas in Fig. 10. In addition to seeing the two distributions in each ISM component, the slope of the satellite's metallicity becomes apparent, particularly through a regression line fit through the cold and dense gas metallicity in the middle panel of Fig. 10. The merging companion galaxy appears to have an upward trend in metallicity, and the fitted line's slope is about  $0.1 \text{ dex Gyr}^{-1}$  in the cold and dense gas. We find that this slope is consistent with self-enrichment from internal star formation in the satellite's main body at a rate of  $\dot{M}_* \sim 0.1 M_{\odot} \text{ yr}^{-1}$ .

## 4 DISCUSSION

### 4.1 Comparison to previous FIRE results

Our results are consistent with previous work in the FIRE simulations. Ma et al. (2016, 2017), which use the FIRE-1 suite of simulations, also find an agreement between the simulated and observed MZR in a wide redshift range. Literature on MW-mass disc galaxies and their gradients can be applied to **m11h**, such as Ma et al. (2017) and Bellardini et al. (2021)'s findings that rotationally supported disc galaxies are more likely to have a negative metallicity gradient, which we see in Fig. 5. While Ma et al. (2017) use a large redshift range of  $z = 0-6$ , El-Badry et al. (2018) supplement these findings, explicitly stating that they found galaxy **m11h** to have significant rotational support around  $z \sim 0$ . Less perturbed galaxies are also found to have flat gradients, as visible in **m11i**, where fewer starbursting events occur, versus the differing gradients of

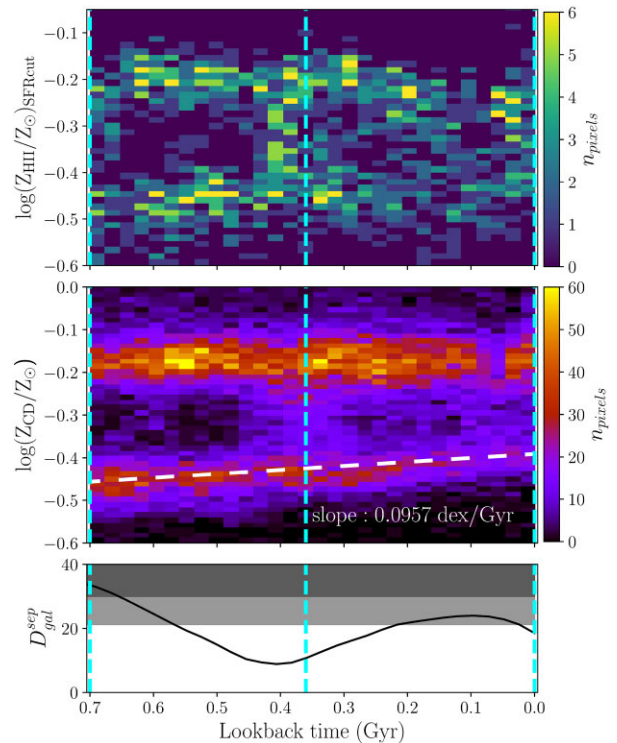


**Figure 10.** Metallicity distribution in nebular regions ( $T \approx 10^4$  K and  $\dot{\Sigma}_*^{10\text{Myr}} > 0$ ) (top panel) and metallicity distribution in cold dense gas ( $T < 500$  K) as a function of time (center panel) for galaxy **m11e**, from  $t_{\text{lookback}} = 0.74 - 0$  Gyr. Bottom panel displays separation distance between the main disc of **m11e** and the merging companion. Cyan lines denote the time of snapshots seen in Fig. 9. The white dashed line represents a least-squares regression of the satellite galaxy's metallicity distribution in the cold and dense gas, where an overall slope of approximately  $0.1 \text{ dex Gyr}^{-1}$  is observed (consistent with internal star formation). Both gas phases show a bimodal distribution resulting from the merger, beginning close to its first appearance in the cold dense gas at  $t \sim 0.67$  Gyr.

**m11d**, **m11e**, and **m11q**, which are all highly perturbed by mergers, starbursts, or metal-poor diffuse gas inflow (Ma et al. 2017; Bellardini et al. 2021).

### 4.2 Inflows, outflows, and feedback: an analysis of metal-mixing models in simulations

#### 4.2.1 The role of feedback

Feedback has a large role to play when considering the results of the MZR. Assuming a so-called closed-box model (i.e. no inflow or outflow of gas into the galaxy), the metal enrichment would be consistent with the integral of the star-formation rate over cosmic time (star formation history). This would give a linear MZR and metal profiles that reflect higher metal content with galaxies/regions of higher star formation rate (Ellison et al. 2008). Further analysis into the extent of the deviation caused by closed-box models uses the distribution of G-dwarfs (typically known as the ‘G-dwarf problem’) in star-forming galaxies (Greener et al. 2021; Spitoni et al. 2021).

However, dwarf galaxy systems are far from closed-box. They are more susceptible to feedback events and therefore prone to outflows, and are more disrupted by mergers and starbursts.

Our findings reflect this; in regards to the MZR, while we find a general linear increase in metallicity with stellar mass, we also find a

large amount of scatter can exist among galaxies of similar masses, and that this scatter is consistent with observations (Sánchez et al. 2019). Merging systems produce the most scatter in both stellar mass and in metallicity. We also find that the FIRE-2 dwarfs are consistent with observations of the median metallicity gradients observed by the MaNGA survey (Belfiore et al. 2017) and that most gradients are flat or slightly negative, although individual observed galaxies seem to exhibit more scatter.

We show that mergers and metal-poor gas inflows produce steeper gradients (e.g. Fig. 5). Our results are again consistent with previous literature in stating that therefore outflows, inflows (Dalcanton 2007; Calura et al. 2009; Kirby et al. 2013; Jimmy et al. 2015; Hidalgo 2017; Escala et al. 2018; Maiolino & Mannucci 2019; Romano et al. 2019), as well as mergers (Kewley et al. 2006; Ellison et al. 2008; Michel-Dansac et al. 2008; Reichard et al. 2009; Ellison et al. 2013; Hopkins et al. 2013; Torres-Flores et al. 2015; Benítez-Llambay et al. 2016; Cortijo-Ferrero et al. 2017; Maiolino & Mannucci 2019), play an important role in the overall metal-content and metal profile of galaxies and in particular are especially important for interpreting metallicity observations of dwarf galaxies.

Finlator & Davé (2008) specifically note the importance of galactic winds, stating that without them, the simulated galaxy metallicities often exceeded those of observations by nearly two to three times. While this result is common in other literature (Calura et al. 2009; Escala et al. 2018; Maiolino & Mannucci 2019), Dalcanton (2007) also rationalizes gas accretion (inflows) as being significant to reducing galaxy metallicity. The role of metal-poor inflows is particularly evident in this study through galaxy **m11q**.

#### 4.2.2 Metal-mixing models

This work further explores the relation between different ISM phases (cold, atomic/molecular, and dense versus warm, ionized, and diffuse) and their metal content. Observationally, it is difficult to probe the cold molecular and atomic gas-phase metallicity as the most common tracers are in the ionized phase (e.g. ionized oxygen) (Krčo et al. 2008; Boselli et al. 2014; Querejeta et al. 2019), though it may be possible to do so using IR observations as in Boselli et al. (2014). Studying the relative abundance of metals in cold gas has important implications for mixing time-scales and the metal content of young stars, since star formation occurs in cold molecular gas and not in warm ionized gas. Overall, we find that all galaxies studied here appear to have a tight correlation in relative enrichment between the cold and dense and nebular ISM phases. Turbulent mixing provides a natural mechanism to quickly diffuse metals from one phase to another. The turbulent cascades measured in different ISM phases via power spectral analysis and other statistics are quite similar (Herron et al. 2016; Pingel et al. 2018; Burkhart 2021), suggesting that these phases are all in the same turbulent cascade and well-mixed (spatially and in dynamical phase-space). This tight correlation breaks down in the outskirts of dwarf galaxies, where almost all of the gas content is ionized and the regions are subjected to metal-poor inflows.

It is commonly known that cosmological simulations require sub-grid models of turbulence and metal diffusion (Escala et al. 2018; Hopkins et al. 2018; Rennehan et al. 2019). A specific comparison of simulations *without* sub-grid diffusion can be found in Escala et al. (2018), and further explored by Rennehan (2021), which ultimately found that metallicity distribution functions (MDFs) with sub-grid diffusion exhibit less scatter. The inclusion of such metal modelling is important to accurately reflect observations in cosmological zoom-in simulations. However, further study by Rennehan (2021) suggests

the sub-grid coefficient is  $\sim 20$  times too low in FIRE. However, mixing on GMC + scales quickly mixes the ISM so long as there is some mixing model, suggesting our results are robust for the most part.

#### 4.3 Metal dependence on SFR

We find that turbulent mixing is important for dwarf galaxies' metallicity profiles and a lack of observed correlation between metals and SFR (see Appendix D; Sánchez et al. 2013, 2015; Sánchez et al. 2017; Blanc et al. 2019; Maiolino & Mannucci 2019; Sharda et al. 2021). Starbursting events (e.g. **m11d**), mergers (e.g. **m11e**), and spiral-like structure (e.g. LMC-like **m11h**) all produce mild negative or flat gradients, and show consistency with metal expectations from inside-out star formation (Krumholz et al. 2018). However, given the short sound-crossing time for dwarf galaxies, mixing is highly efficient and quickly acts to flatten metal gradients (see Fig. C2). Regions of moderate to low SFR have no correlation with metal content and more scatter exists between cold and nebular gas.

This follows with some disagreement in other studies. Blanc et al. (2019) find in their analysis of the MZR (in both dwarf and high-mass galaxies) that the shape of the MZR is *not* influenced by a secondary dependence on SFR. Other studies that do not find a dependence on SFR are Sánchez et al. (2013, 2015, 2017).

On the other hand, Sanders et al. (2021) find that in addition to evolving with redshift ( $z = 3.3 - 0$ ), the MZR therefore also evolves as a function of SFR, as does Hidalgo (2017), which states that the SFR can play a significant role in the observed shape of the MZR over redshifts  $0 < z < 3$ . However, we note that these studies cover either a larger or higher redshift range (and sometimes both), whereas this paper only examines simulated dwarf galaxies around the local Universe ( $z = 0.11 - 0$ ). The strongest correlations tends to be observed only in regions of high SFR (Lara-López et al. 2010; Salim et al. 2014; Maier et al. 2015; Telford et al. 2016; Sánchez et al. 2019).

#### 4.4 Comparison to the Magellanic Clouds

Throughout our analysis of these five FIRE-2 dwarf galaxies, we make repeated comparisons with the SMC and LMC. Our simulations lie within the approximate ranges of SMC-mass to twice that of the LMC (in terms of stellar mass), with the SMC mass taken from Bekki & Stanimirović (2009) and LMC from van der Marel et al. (2002). Knowing this allows us to determine that the corresponding star formation rates in the simulations are not unrealistic. Derived primarily from UV observations that correlate with our 40-Myr averaged SFR (see Lee et al. (2009) for a comparison of discrepancies between  $H\alpha$  versus UV SFRs of dwarf galaxies), the SMC has the higher SFR of the two magellanic clouds (MCs) at  $0.3 M_{\odot} \text{yr}^{-1}$  (Rezaei Kh. et al. 2014; Rubele et al. 2015; Hagen et al. 2017), whereas the LMC is about  $0.2 M_{\odot} \text{yr}^{-1}$  (Harris & Zaritsky 2009; Rezaei Kh. et al. 2014). We see that while the LMC exhibits a lower SFR than the SMC, there is not a corresponding relation between our SMC-mass and LMC-mass simulations. Instead, the simulations near LMC-mass (**m11d** and **m11h**, respectively) also have the highest consistent rates of star formation of the five galaxies. This suggests the importance of considering the SMC's interaction with the Milky Way and LMC (Weinberg 2000).

None of these FIRE-2 dwarfs are explicitly SMC-mass, with the closest being **m11q** at approximately  $10^{8.8} M_{\odot}$ , but there does not appear to be any significant differences between our sample and the MCs.

## 5 CONCLUSIONS

In this paper, we presented an analysis of spatially resolved gas-phase metallicity relations for five FIRE-2 dwarf galaxies with masses comparable to the Magellanic Clouds. We investigated metallicity distributions across several different ISM phases, the gas-phase mass–metallicity relation, metallicity profiles and gradients, the relative enrichment between the ISM phases, and examined a brief case study of a major-merger in one run (**m11e**). We can summarize our findings by the following key takeaways:

(i) All five FIRE-2 dwarf galaxies match the observable gas phase MZR. We see falling metallicities in time in **m11e** (explained by the merging metal-poor satellite galaxy) and **m11q** (reasoned through the accretion of metal-poor ionized gas). The three other galaxies, **m11d**, **m11h**, and **m11i**, all have a positive slope of evolution in the MZR plane and are similar to each other in that regard.

(ii) Metallicity in nebular regions (H II gas with non-zero 10 Myr SFR) closely traces and is predictive of metals in the cold and dense gas component, resulting in a typical scatter of  $\pm 0.1$  dex.

(iii) Any difference in relative enrichment outside of  $\pm 0.1$  dex (up to 0.7 dex in the cold and dense gas for **m11d**, and 0.5 dex in the H II gas for **m11q**, for example) can be attributed to large-scale dynamics of the ISM, like metal-poor gas inflows or galaxy-scale starbursts, as seen in Fig. 8. The local SFR is not driving higher enrichment in the nebular gas versus the cold and dense gas component (see Fig. D1).

(iv) All five simulated galaxies exhibit flat to slightly negative metallicity gradients, and are consistent with observations from Tremonti et al. (2004), Belfiore et al. (2017), and Sánchez et al. (2019).

(v) The merging companion in **m11e** results in an increased stellar mass, but a drop in average gas-phase metallicity as the metal-poor satellite begins to incorporate itself into the main body.

Overall, the FIRE-2 dwarf galaxies have diverse features and morphologies, including LMC-mass galaxies that are extremely bursty (**m11d**), discy (**m11h**), undergoing a major-merger (**m11e**), SMC-mass and static (**m11i**), or undergoing large amounts of accretion (**m11q**). Our results build upon previous literature explaining the importance of the MZR and metallicity profiles to understanding gas reservoirs and galaxy evolution, highlighting the importance of considering cosmological context in metallicity relations at low redshifts.

While our results match observations, this study only consists of five galaxies representative of the local Universe ( $z \sim 0$ ). With the recent launch and deployment of the *James Webb Space Telescope*, it will be possible to compare high-redshift galactic simulations to observations at an unprecedented level of resolution. Future study into the formation history of dwarf galaxies at high redshifts would provide a more quantitative understanding of whether simulations can accurately reproduce metallicity scaling relations seen in observations during the peak of star formation in the dwarf galaxy regime.

## ACKNOWLEDGEMENTS

The authors would like to thank the anonymous referee for providing comments and suggestions that improved the quality of the manuscript. LEP is grateful to the University of Louisville’s Brown Fellows Program for financial support, funded by the James Graham Brown Foundation. LEP is also thankful to the Flatiron Institute for continued financial support and resources. BB is grateful for generous support by the David and Lucile Packard Foundation and Alfred P. Sloan Foundation. AW received support from: National

Science Foundation via CAREER award AST-2045928 and grant AST-2107772; National Aeronautics and Space Administration ATP grant 80NSSC20K0513; *HST* grants AR-15809 and GO-15902 from the Space Telescope Science Institute.

## DATA AVAILABILITY

The data supporting the plots within this article are available on reasonable request to the corresponding author. A public version of the GIZMO code is available at <http://www.tapir.caltech.edu/~phopkin/Site/GIZMO.html>. Additional data including simulation snapshots, initial conditions, and derived data products are available at <https://fire.northwestern.edu/data/>. The FIRE-2 simulations are publicly available (Wetzel et al. 2022) at <http://flathub.flatironinstitute.org/fire>.

## REFERENCES

- Andrews B. H., Martini P., 2013, *ApJ*, 765, 140
- Asari N. V., Cid Fernandes R., Stasińska G., Torres-Papaqui J. P., Mateus A., Sodré L., Schoenell W., Gomes J. M., 2007, *MNRAS*, 381, 263
- Barnes J. E., 2004, *MNRAS*, 350, 798
- Behroozi P. S., Wechsler R. H., Conroy C., 2013, *ApJ*, 770, 57
- Bekki K., Stanimirović S., 2009, *MNRAS*, 395, 342
- Belfiore F. et al., 2017, *MNRAS*, 469, 151
- Bellardini M. A., Wetzel A., Loebman S. R., Faucher-Giguère C.-A., Ma X., Feldmann R., 2021, *MNRAS*, 505, 4586
- Bemis A., Wilson C. D., 2019, *AJ*, 157, 131
- Benítez-Llambay A., Navarro J. F., Abadi M. G., Gottlöber S., Yepes G., Hoffman Y., Steinmetz M., 2016, *MNRAS*, 456, 1185
- Blanc G. A., Lu Y., Benson A., Katsianis A., Barraza M., 2019, *ApJ*, 877, 6
- Boselli A., Cortese L., Boquien M., Boissier S., Catinella B., Gavazzi G., Lagos C., Saintonge A., 2014, *A&A*, 564, A67
- Burkhart B., 2021, *PASP*, 133, 102001
- Burkhart B., Stanimirović S., Lazarian A., Kowal G., 2010, *ApJ*, 708, 1204
- Calura F., Menci N., 2009, *MNRAS*, 400, 1347
- Calura F., Pipino A., Chiappini C., Matteucci F., Maiolino R., 2009, *A&A*, 504, 373
- Cortijo-Ferrero C. et al., 2017, *A&A*, 607, A70
- Dalcanton J. J., 2007, *ApJ*, 658, 941
- Dekel A., Silk J., 1986, *ApJ*, 303, 39
- Draine B. T., 2011, *Physics of the Interstellar and Intergalactic Medium*. Vol. 148. Princeton Univ. Press, Princeton
- El-Badry K., Wetzel A., Geha M., Hopkins P. F., Kereš D., Chan T. K., Faucher-Giguère C.-A., 2016, *ApJ*, 820, 131
- El-Badry K. et al., 2018, *MNRAS*, 473, 1930
- Ellison S. L., Patton D. R., Simard L., McConnachie A. W., 2008, *ApJ*, 672, L107
- Ellison S. L., Mendel J. T., Patton D. R., Scudder J. M., 2013, *MNRAS*, 435, 3627
- Escala I. et al., 2018, *MNRAS*, 474, 2194
- Finlator K., Davé R., 2008, *MNRAS*, 385, 2181
- Gallazzi A., Charlot S., Brinchmann J., White S. D. M., Tremonti C. A., 2005, *MNRAS*, 362, 41
- Gibson B. K., Pilkington K., Brook C. B., Stinson G. S., Bailin J., 2013, *A&A*, 554, A47
- Greener M. J., Merrifield M., Aragón-Salamanca A., Peterken T., Andrews B., Lane R. R., 2021, *MNRAS*, 502, L95
- Hagen L. M., Siegel M. H., Hoversten E. A., Gronwall C., Immler S., Hagen A., 2017, *MNRAS*, 466, 4540
- Harris J., Zaritsky D., 2009, *AJ*, 138, 1243
- Hemler Z. S. et al., 2021, *MNRAS*, 506, 3024
- Herron C. A., Burkhart B., Lazarian A., Gaensler B. M., McClure-Griffiths N. M., 2016, *ApJ*, 822, 13
- Hidalgo S. L., 2017, *A&A*, 606, A115
- Hirschmann M., De Lucia G., Fontanot F., 2016, *MNRAS*, 461, 1760

- Hopkins P. F. et al., 2018, *MNRAS*, 480, 800
- Hopkins P. F., Cox T. J., Hernquist L., Narayanan D., Hayward C. C., Murray N., 2013, *MNRAS*, 430, 1901
- Iwamoto K., Brachwitz F., Nomoto K., Kishimoto N., Umeda H., Hix W. R., Thielemann F.-K., 1999, *ApJS*, 125, 439
- Jimmy Tran K. V., Saintonge A., Accurso G., Brough S., Oliva-Altamirano P., 2015, *ApJ*, 812, 98
- Karl S. J., Naab T., Johansson P. H., Kotarba H., Boily C. M., Renaud F., Theis C., 2010, *ApJ*, 715, L88
- Kennicutt R. C., Evans N. J., 2012, *ARA&A*, 50, 531
- Kewley L. J., Ellison S. L., 2008, *ApJ*, 681, 1183
- Kewley L. J., Geller M. J., Barton E. J., 2006, *AJ*, 131, 2004
- Kirby E. N., Cohen J. G., Guhathakurta P., Cheng L., Bullock J. S., Gallazzi A., 2013, *ApJ*, 779, 102
- Köppen J., Weidner C., Kroupa P., 2007, *MNRAS*, 375, 673
- Krčo M., Goldsmith P. F., Brown R. L., Li D., 2008, *ApJ*, 689, 276
- Krumholz M. R., Gnedin N. Y., 2011, *ApJ*, 729, 36
- Krumholz M. R., Burkhardt B., Forbes J. C., Crocker R. M., 2018, *MNRAS*, 477, 2716
- Lahen N., Johansson P. H., Rantala A., Naab T., Frigo M., 2018, *MNRAS*, 3958, 3934
- Lanfranchi G., Matteucci F., 2003, *MNRAS*, 345, 71
- Lanfranchi G. A., Matteucci F., 2007, *A&A*, 468, 927
- Lanfranchi G. A., Matteucci F., 2010, *A&A*, 512, A85
- Lara-López M. A. et al., 2010, *A&A*, 521, A85
- Lee H., Bell E. F., Somerville R. S., 2008, Proc. IAU Symp. 255, Low-Metallicity Star Formation: From the First Stars to Dwarf Galaxies. Kluwer, Dordrecht, p. 100
- Lee D.-H. et al., 2006, *ApJ*, 644, L181
- Lee J. C. et al., 2009, *ApJ*, 706, 599
- Leitherer C. et al., 1999, *ApJS*, 123, 3
- Leitherer C., Ekström S., Meynet G., Schaerer D., Agienko K. B., Levesque E. M., 2014, *ApJS*, 212, 14
- Ma X., Hopkins P. F., Faucher-Giguère C.-A., Zolman N., Muratov A. L., Kereš D., Quataert E., 2016, *MNRAS*, 456, 2140
- Ma X., Hopkins P. F., Feldmann R., Torrey P., Faucher-Giguère C.-A., Kereš D., 2017, *MNRAS*, 466, 4780
- Magrini L., Coccato L., Stanghellini L., Casasola V., Galli D., 2016, *A&A*, 588, A91
- Maier C., Ziegler B. L., Lilly S. J., Contini T., Pérez-Montero E., Lamareille F., Bolzonella M., Le Floch E., 2015, *A&A*, 577, A14
- Maiolino R., Mannucci F., 2019, *A&AR*, 27, 3
- Maiolino R. et al., 2008, *A&A*, 488, 463
- Mercado F. J. et al., 2021, *MNRAS*, 501, 5121
- Michel-Dansac L., Lambas D. G., Alonso M. S., Tissera P., 2008, *MNRAS*, 386, L82
- Mozer B. P., Naab T., White S. D. M., 2013, *MNRAS*, 428, 3121
- Mo H. J., Mao S., White S. D. M., 1998, *MNRAS*, 295, 319
- Nomoto K., Tominaga N., Umeda H., Kobayashi C., Maeda K., 2006, *Nucl. Phys. A*, 777, 424
- Orr M. E. et al., 2020, *MNRAS*, 496, 1620
- Pagel B. E. J., Edmunds M. G., Fosbury R. A. E., Webster B. L., 1978, *MNRAS*, 184, 569
- Patel P. B., Loebman S. R., Wetzel A., Faucher-Giguère C.-A., El-Badry K., Bailin J., 2022, *MNRAS*, 512, 5671
- Pawlik A. H., Milosavljević M., Bromm V., 2013, *ApJ*, 767, 59
- Pérez-González P. G. et al., 2008, *ApJ*, 675, 234
- Pilkington K. et al., 2012, *A&A*, 540, A56
- Pingel N. M., Lee M.-Y., Burkhardt B., Stanimirović S., 2018, *ApJ*, 856, 136
- Querejeta M. et al., 2019, *A&A*, 625, A19
- Read A. M., 2003, *MNRAS*, 342, 715
- Reichard T. A., Heckman T. M., Rudnick G., Brinchmann J., Kauffmann G., Wild V., 2009, *ApJ*, 691, 1005
- Rennehan D., 2021, *MNRAS*, 506, 2836
- Rennehan D., Babul A., Hopkins P. F., Davé R., Moa B., 2019, *MNRAS*, 483, 3810
- Rezaei Kh. S., Javadi A., Khosroshahi H., Van Loon J. T., 2014, *MNRAS*, 445, 2214
- Roman-Duval J. et al., 2019, *ApJ*, 871, 151
- Romano D., Starkeburg E., 2013, *MNRAS*, 434, 471
- Romano D., Calura F., D’Ercole A., Few C. G., 2019, *A&A*, 630, A140
- Rubele S. et al., 2015, *MNRAS*, 449, 639
- Russell S. C., Dopita M. A., 1992, *ApJ*, 508, 384
- Sacchi E. et al., 2016, *ApJ*, 830, 3
- Salim S., Lee J. C., Ly C., Brinchmann J., Davé R., Dickinson M., Salzer J. J., Charlot S., 2014, *ApJ*, 797, 126
- Sánchez S. F. et al., 2013, *A&A*, 554, A58
- Sánchez S. et al., 2015, *Galaxies*, 3, 164
- Sánchez S. F. et al., 2019, *MNRAS*, 484, 3042
- Sánchez S. F., Heckman T., Blanc G. A., 2017, *ApJ*, 844, 80
- Sanders R. L. et al., 2021, *ApJ*, 914, 19
- Sawala T., Scannapieco C., Maio U., White S., 2010, *MNRAS*, 402, 1599
- Sharda P., Krumholz M. R., Wisnioski E., Acharyya A., Federrath C., Forbes J. C., 2021, *MNRAS*, 504, 53
- Shaver P. A., McGee R. X., Newton L. M., Danks A. C., Pottasch S. R., 1983, *MNRAS*, 204, 53
- Shen S., Wadsley J., Stinson G., 2010, *MNRAS*, 407, 1581
- Simon J. D., 2019, *ARA&A*, 57, 375
- Spitoni E., Calura F., Mignoli M., Gilli R., Silva Aguirre V., Gallazzi A., 2020, *A&A*, 642, A113
- Spitoni E., Calura F., Silva Aguirre V., Gilli R., 2021, *A&A*, 648, L5
- Su K.-Y., Hopkins P. F., Hayward C. C., Faucher-Giguère C.-A., Kereš D., Ma X., Robles V. H., 2017, *MNRAS*, 471, 144
- Telford O. G., Dalcanton J. J., Skillman E. D., Conroy C., 2016, *ApJ*, 827, 35
- Tolstoy E., Hill V., Tosi M., 2009, *ARA&A*, 47, 371
- Toribio San Cipriano L., Domínguez-Guzmán G., Esteban C., García-Rojas J., Mesa-Delgado A., Bresolin F., Rodríguez M., Simón-Díaz S., 2017, *MNRAS*, 467, 3759
- Torres-Flores S., Mendes de Oliveira C., Amram P., Alfaro-Cuello M., Carrasco E. R., de Mello D. F., 2015, *ApJ*, 798, L24
- Torrey P., Cox T. J., Kewley L., Hernquist L., 2012, *ApJ*, 746, 108
- Tremonti C. A. et al., 2004, *ApJ*, 613, 898
- Tsuge K., Tachihara K., Fukui Y., Sano H., Tokuda K., Ueda J., Iono D., 2021, *PASJ*, 73, 417
- van der Marel R. P., Alves D. R., Hardy E., Suntzeff N. B., 2002, *AJ*, 124, 2639
- Velázquez J. A. F. et al., 2020, *MNRAS*, 13, 1
- Wang X. et al., 2019, *ApJ*, 882, 94
- Weinberg M. D., 2000, *ApJ*, 532, 922
- Wetzel A. et al., 2022, preprint ([arXiv:2202.06969](https://arxiv.org/abs/2202.06969))
- Wiersma R. P. C., Schaye J., Theuns T., Dalla Vecchia C., Tornatore L., 2009, *MNRAS*, 399, 574
- Yates R. M., Henriques B., Thomas P. A., Kauffmann G., Johansson J., White S. D. M., 2013, *MNRAS*, 435, 3500
- Yin J., Matteucci F., Vladilo G., 2011, *A&A*, 531, A136
- Zahid H. J., Bresolin F., Kewley L. J., Coil A. L., Davé R., 2012, *ApJ*, 750, 120

## APPENDIX A: METALLICITY MAPS RELATIVE TO $\bar{Z}$

We present figures with metallicity colourbars scaled by the mean mass-weighted metallicity of each galaxy. While this is not a standard practice, it aids in distinguishing the metallicity gradients and deviations within each galaxy in Figs 2 and 3, seen here as Figs A1 and A2.

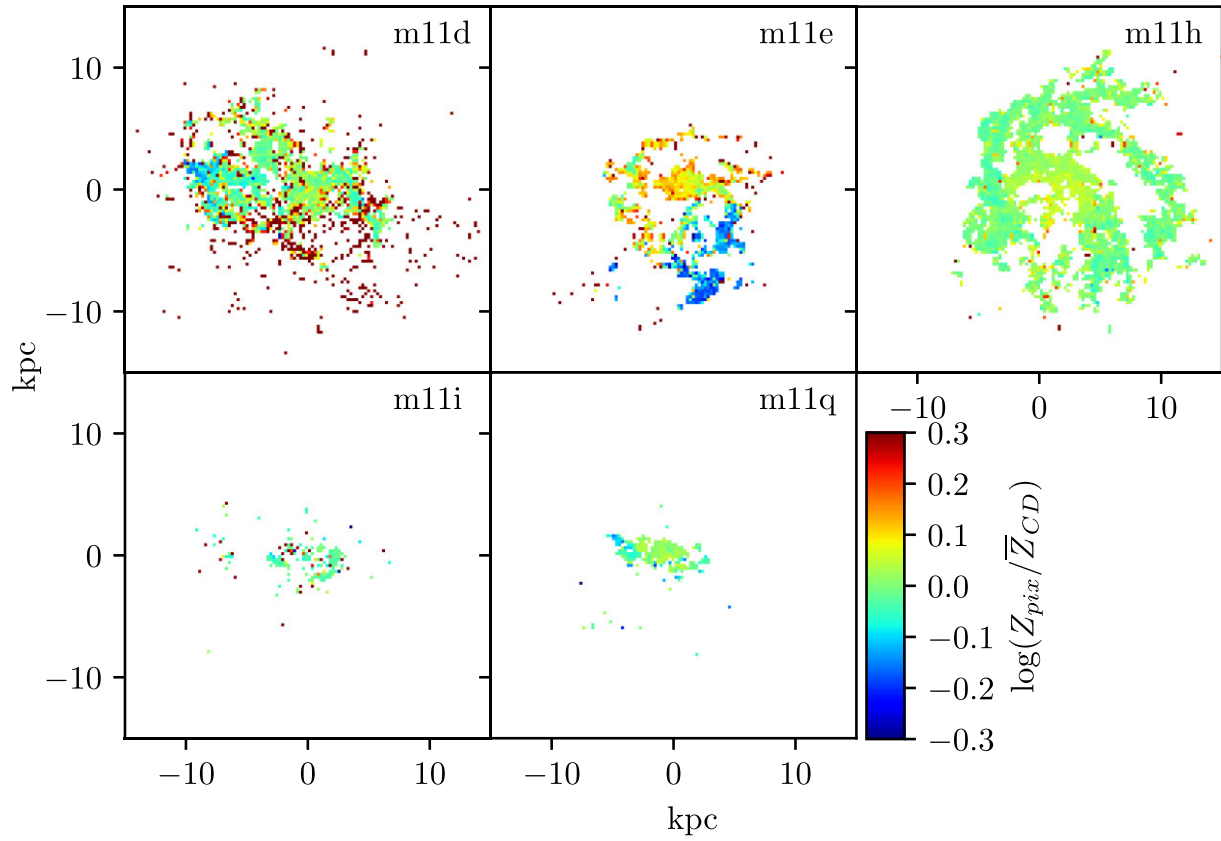


**Figure A1.** Spatial distributions of metallicity of cold and dense gas component ( $T < 500$  K) of FIRE-2 galaxies with a pixel size of 250 pc, coloured by their metallicity relative to the mean metallicity at  $t_{\text{lookback}} \approx 0.36$  Gyr.

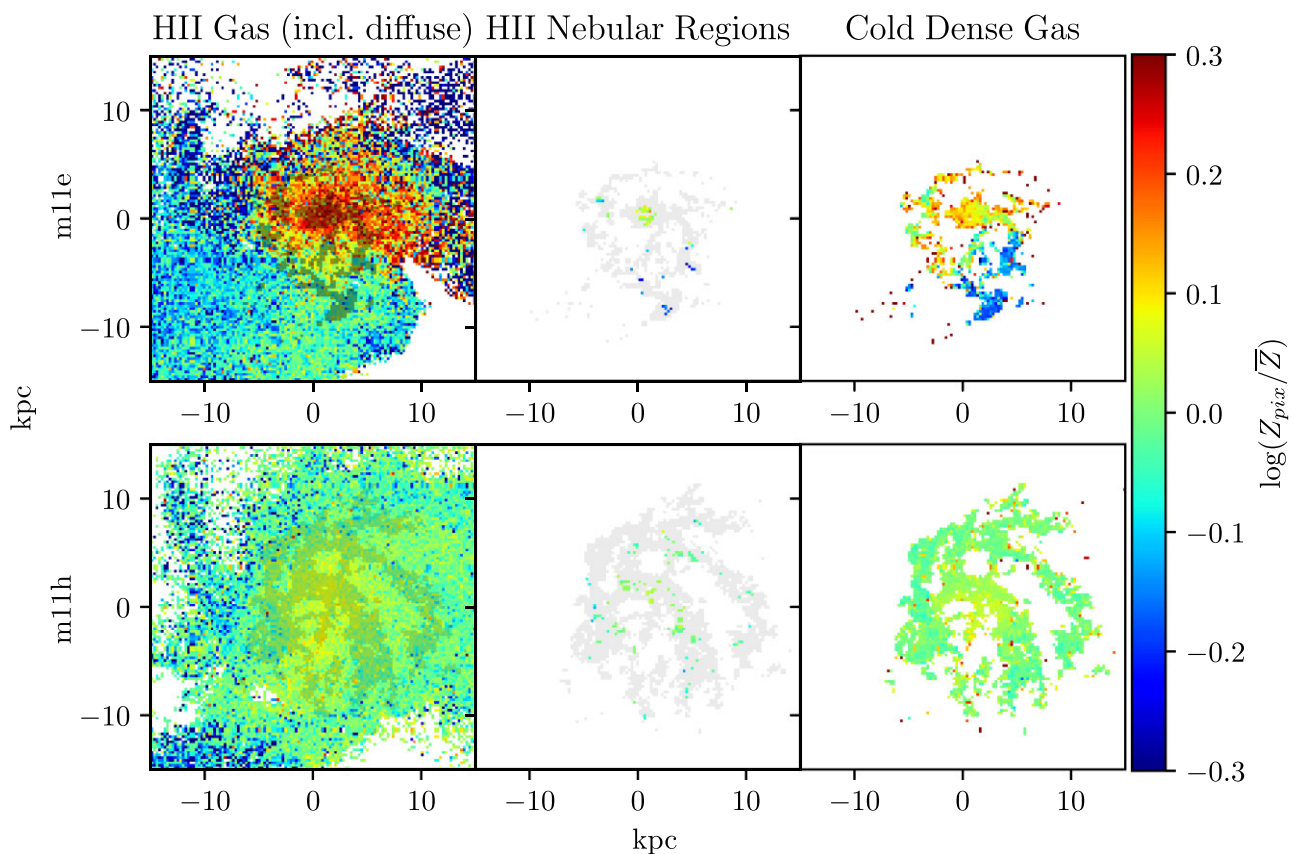


**Figure A2.** Spatial distributions of metallicity of diffuse H II gas (left column), nebular regions (middle column), and cold and dense gas component (right column) for two of the FIRE-2 dwarf galaxies, **m11e** (top row) and **m11h** (bottom row) coloured as Fig. A1.

## APPENDIX B: METALLICITY PROFILES AND MZGR IN H II

Here, we present the metallicity profiles and gradients as a function of stellar mass (as in Figs 5 and 6) for the nebular regions in Figs B1 and B2. Though qualitatively similar, there is significantly more

snapshot-to-snapshot scatter in the overall gradients in the lower mass galaxies (particularly **m11e** and **m11q**). This is largely due to the low SFRs (i.e. small number of pixels contributes to the gradient calculation) and the large flux of warm gas, either in the halo–halo interaction in the merger for **m11e** or the gas accretion for **m11q**.

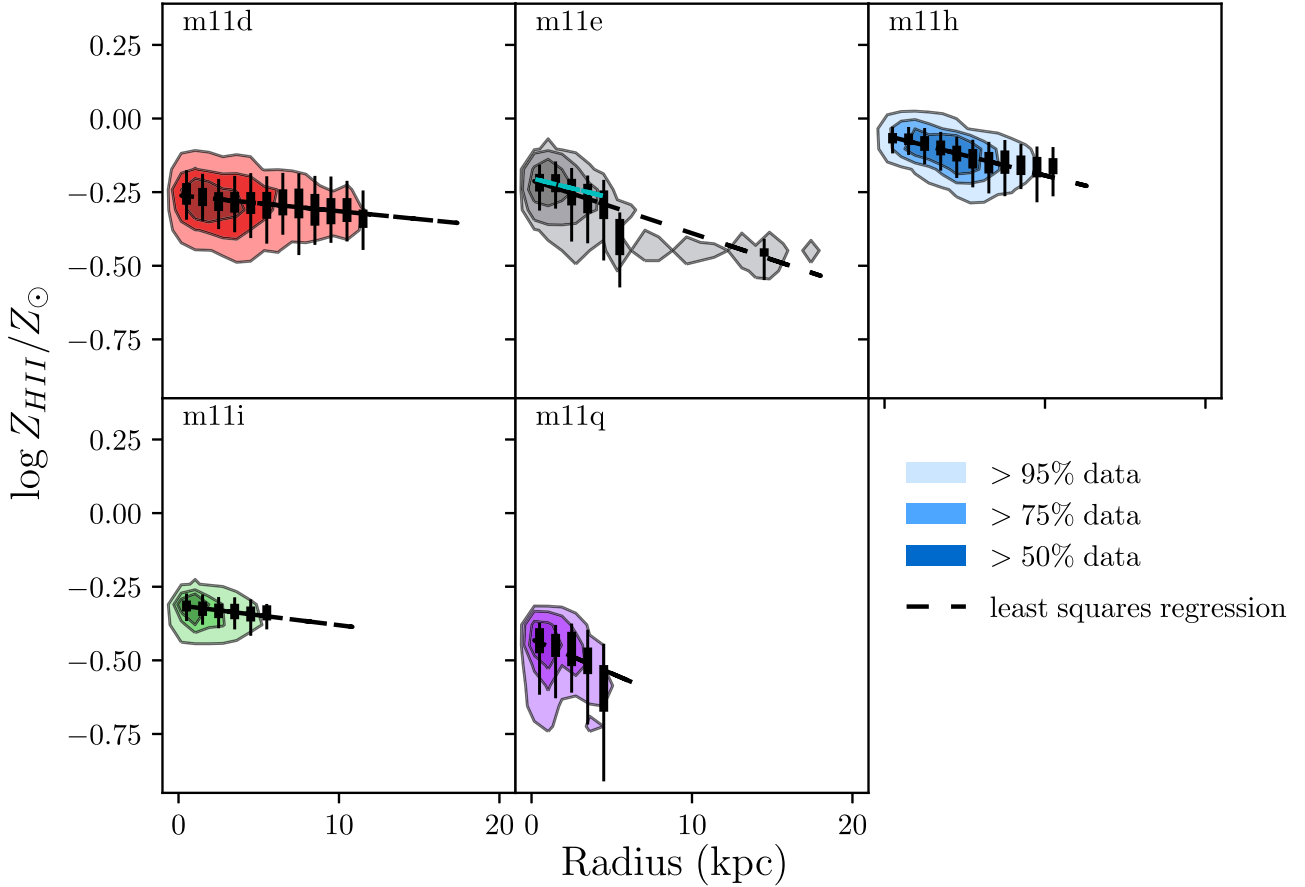


**Figure B1.** Metallicity profiles in the ionized gas (with recent star formation) of the five galaxies analysed here with 250 pc pixel size, where distribution contains all pixels of the corresponding galaxy across all snapshots ( $t_{\text{lookback}} = 1.4\text{--}0$  Gyr,  $0 < z < 0.11$ ). Shaded regions represent 50, 75, and 95 per cent of data. Colours are as Fig. 1 and box and whiskers are as Fig. 4. The least-squares regression, denoted by the dashed black line, is fit through the entire distribution with the exception of **m11e**, where an additional cyan line has been plotted through only the main galaxy body ( $R > 5$  kpc and  $t < 0.83$  Gyr). *Upper-left:* galaxy **m11d**; majorly disrupted due to starbursts with a negative metallicity gradient. *Centre-top:* galaxy **m11e**; apparent steep metallicity gradient due to the merging companion. See cyan line for fit of main galaxy body. Both fits appear identical due to the ionized gas regions extending much farther and therefore mixing much earlier than their cold and dense counterparts. *Upper-right:* galaxy **m11h**; appears to be an LMC-mass spiral with inside-out growth; slight metallicity gradient most consistent with such growth models. *Lower-left:* galaxy **m11i**; slight gradient owing to very well-mixed nature. *Centre-bottom:* galaxy **m11q**; very steep gradient possibly due to metal-poor inflows that significantly affect the galaxy due to its small size and mass.

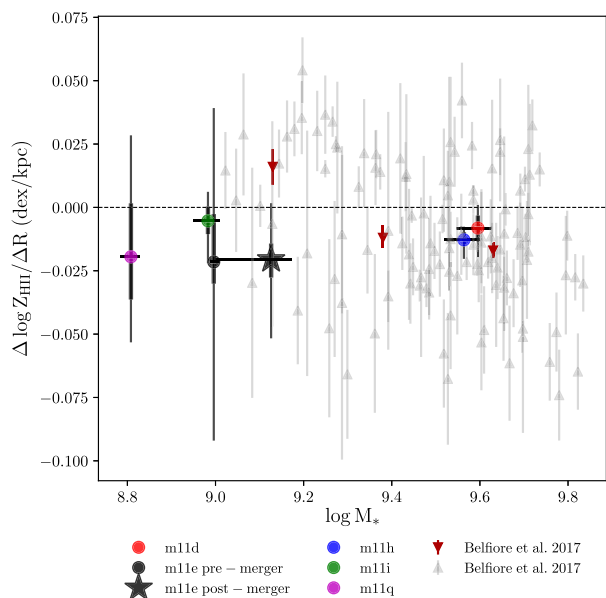


**Figure B2.** Ionized gas (with recent star formation) metallicity gradients as a function of stellar mass for all FIRE-2 dwarfs, averaged over the entire analysis period ( $t_{\text{lookback}} = 1.4 - 0$  Gyr,  $0 < z < 0.11$ ), with **m11e** being split into pre-merger (circle) and post-merger (star). Points denote the position of the galaxy’s average stellar mass and average slope of metallicity gradient in dex per kpc (displayed in Fig. 5). Thick vertical bars denote 25–75 per cent of data within that interval and thin vertical bars represent 5–95 per cent of data. Thick horizontal bars represent the change in stellar mass, with the leftmost point being the first snapshot and the rightmost point depicting the last snapshot. Colours are as Fig. 1. Grey points and burgundy points and errorbars are observational data in the MaNGA survey from Belfiore et al. (2017; their fig. B1), where grey points are individual galaxies and red points are the median values of 0.25 dex stellar mass bins. Galaxies primarily have a weak to negative gradient; they may exhibit a positive slope shortly after starbursts, as in the case of **m11d**. **m11e** clearly has a gradient similar to that of **m11h** and **m11i** before its merger. Simulations are in good agreement with observations.

## APPENDIX C: DIFFERENTIAL ENRICHMENT DISTANCE (DED)

In Fig. 7, we found that the metallicity of the cold and dense gas and the ionized gas phases were nearly identical (within  $\pm 0.1$  dex). However, we also explore this by the differential enrichment distance (DED).

$$\text{DED} = \frac{\log Z_{\text{CD}}/Z_{\odot} - \log Z_{\text{HII}}/Z_{\odot}}{\sqrt{2}} \quad (\text{C1})$$

A positive DED value indicates higher local enrichment in the cold and dense gas, while a negative DED value indicates higher local enrichment in the ionized gas.

We show the distribution of the DED in each of the galaxies, as a function of gas surface density and star formation rate surface density, in Figs C1 and C2. We conclude that the cold and dense gas appears to almost always be slightly more enriched than the ionized gas on average. We find no significant correlation with the DED and other physical factors such as velocity dispersion, gas surface density, and star formation rate.

We note that for the nebular regions there does not appear to be a significant relationship for the cold and dense gas surface density or 40 Myr-averaged SFR. We see a slight striation pattern in the latter (purely an effect of resolution, i.e. counting individual young star particles), but neither seem to show any significant relationships aside from the fact that cold and dense gas is slightly more enriched, despite the SFR and gas surface density.

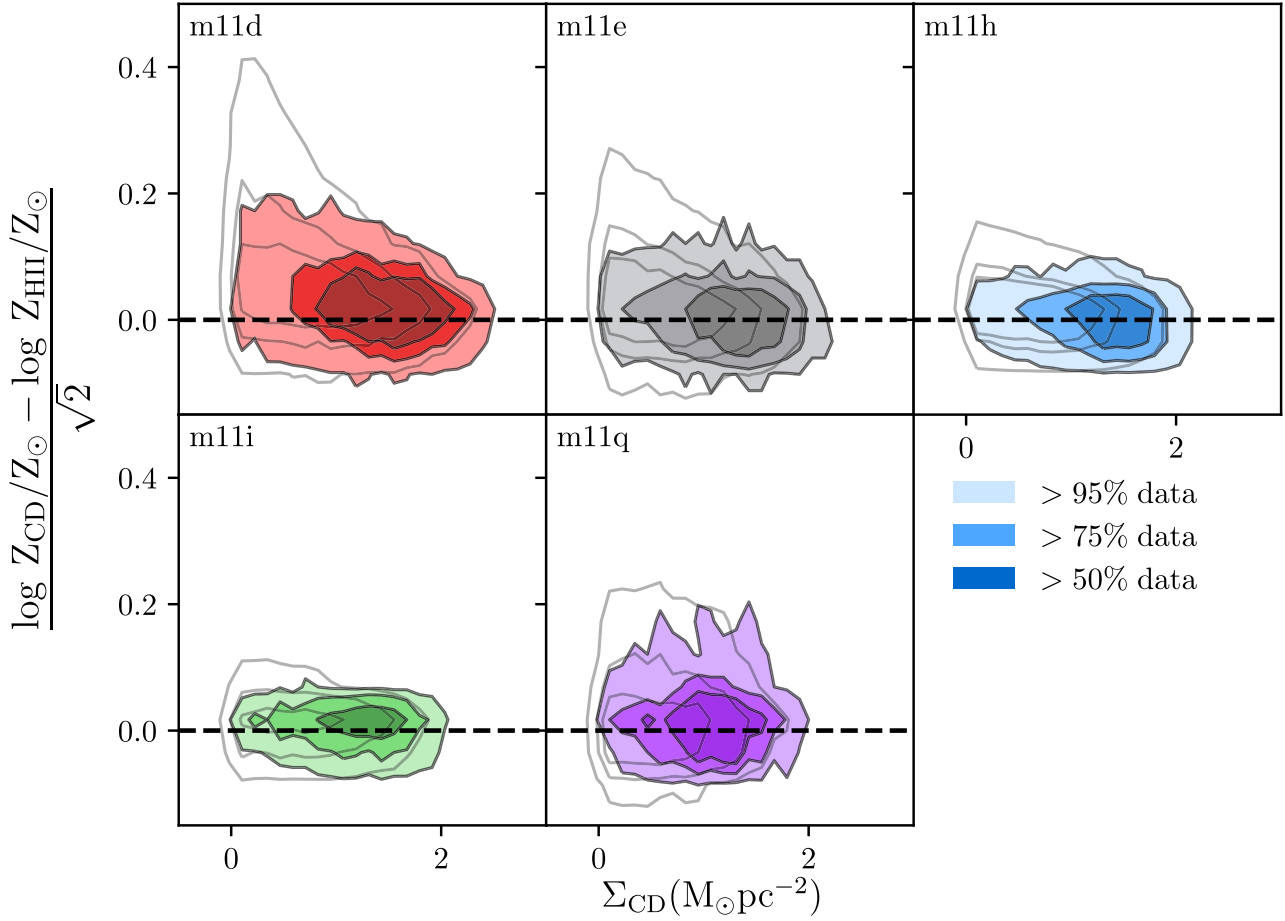


**Figure C1.** Comparing the distribution of cold and dense gas surface density to the relative DED for all five FIRE-2 dwarf galaxies at all snapshots ( $t_{\text{lookback}} = 1.4 - 0$  Gyr,  $0 < z < 0.11$ ). Filled contours denote 50, 75, and 95 per cent of data inclusion in nebular regions; unfilled contours represent the H II gas with diffuse component (does not require recent star formation). Dashed black line represents equal enrichment in both the H II gas and the cold dense gas. Colours are as Fig. 1. The filled contours (observable) appear to be roughly equally enriched, except for **m11d** and **m11i**, the two galaxies with the most starburst activity. The biggest scatters exist at low surface density and are not evident in the nebular regions. No general dependence on the differential enrichment as a function of cold and dense gas surface density is seen in any of the simulations.

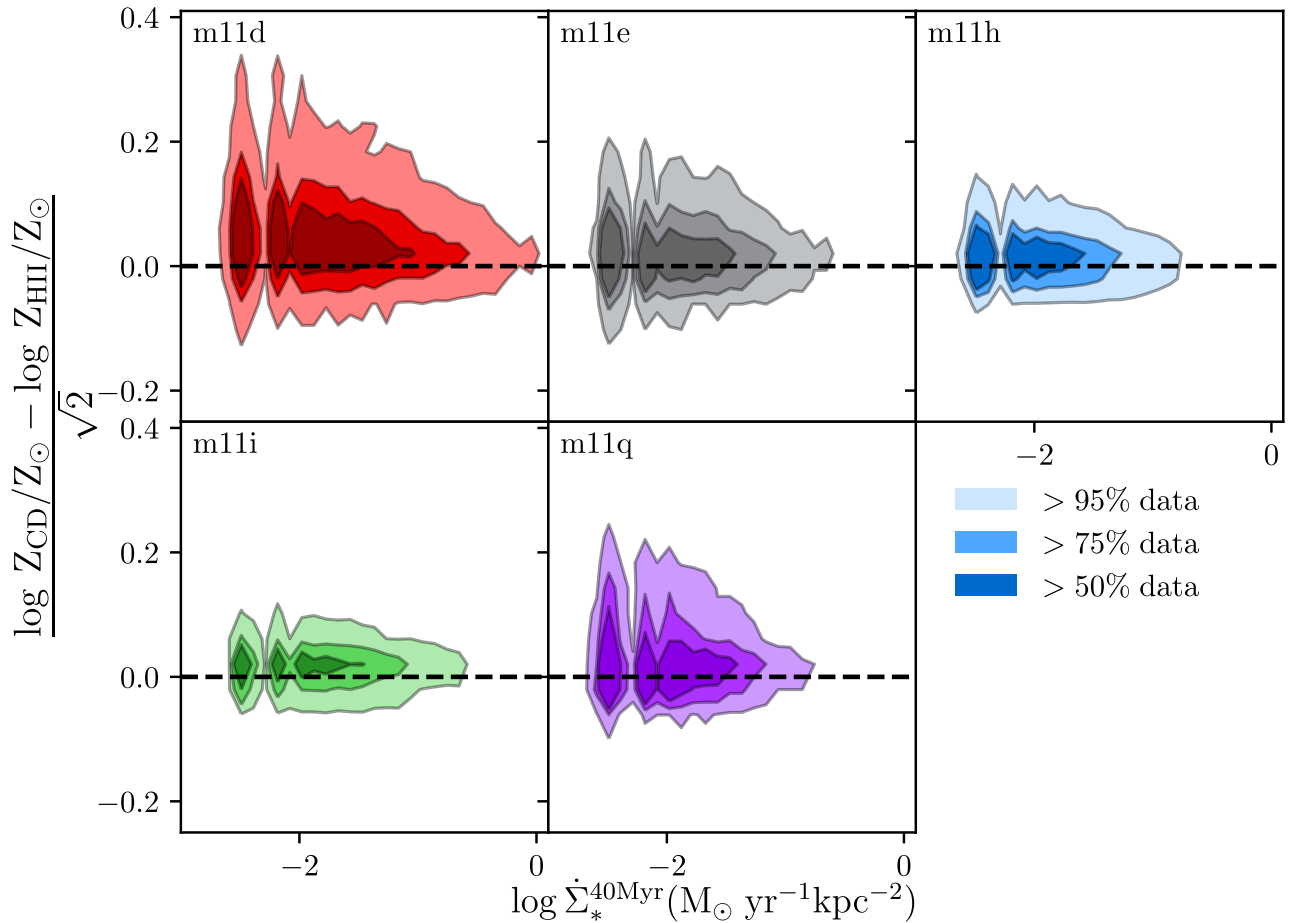


**Figure C2.** Comparing the distribution of star formation rate surface density (averaged over the last 40 Myr) to the DED for all five galaxies, in the style of Fig. C1, for all snapshots ( $t_{\text{lookback}} = 1.4 - 0$  Gyr,  $0 < z < 0.11$ ). Filled contours denote 50, 75, and 95 per cent of data inclusion, including diffuse components. Colours as Fig. 1. All distributions appear to be unbiased, with the exception of **m11d**. No general dependence on the differential enrichment as a function of SFR is seen in any of the simulations.

#### APPENDIX D: RELATING METALLICITY TO STAR FORMATION

During this study, an effort was made to correlate the local star formation rate, metallicity, and effective radius in these five FIRE-2 dwarf galaxies. This can be found in Fig. D1, where we represent the star formation rate’s surface density (averaged over the last 40 Myr, in units of  $M_{\odot}\text{yr}^{-1}\text{pc}^{-2}$ ), plotted against the log of the

total solar metallicity in the cold and dense gas. There appears to be no relationship in any of the five galaxies between these two quantities, with no further dependence on the effective radius as well. We note that while galaxy **m11e** appears to have a smaller, mirrored distribution at lower metallicity and higher radius, that this is likely from the snapshots of the merging companion, which intuitively explain the high radius and low-metallicity values.

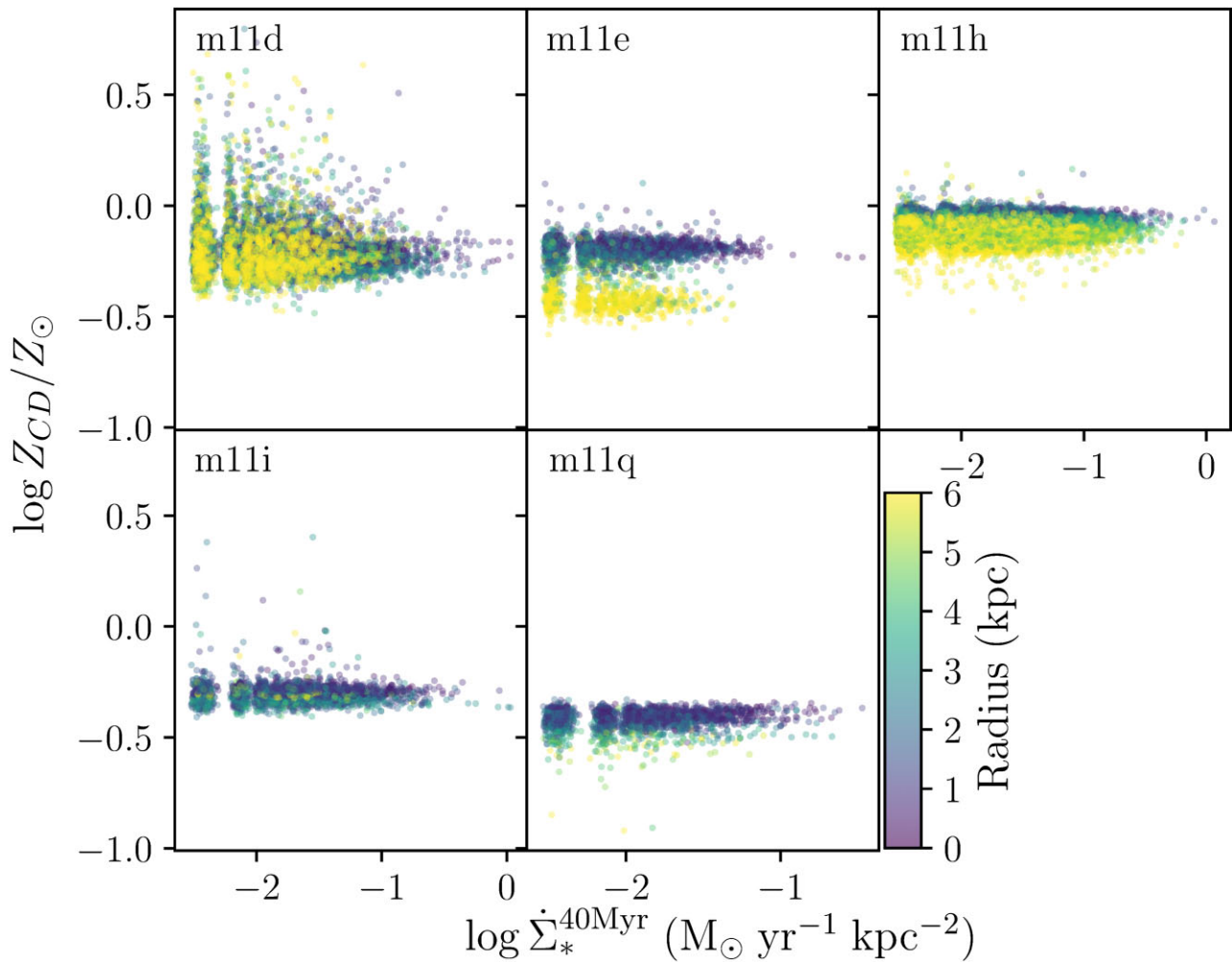


**Figure D1.** Distribution of the star formation rate surface density (averaged over the last 40 Myr) compared to the total solar metallicity in the cold and dense gas for all five galaxies, from all snapshots ( $t_{\text{lookback}} = 1.4 - 0$  Gyr,  $0 < z < 0.11$ ). The colour of pixels is determined by the radius in kpc. All distributions appear to have little-to-no correlation between the quantities.

This paper has been typeset from a  $\text{\TeX}/\text{\LaTeX}$  file prepared by the author.